The Responses of High Latitude Clouds and High and Mid-Latitude Surface Pressures to the Solar Wind Sector Structure.

Brian A Tinsley[1], Limin Zhou[2], Lin Wang[2] and Liang Zhang[2]

[1]University of Texas at Dallas, Dallas, TX USA, [2]East China Normal University, Shanghai, China.

Abstract

The opacity of clouds at Alert, Canada, Summit, Greenland, and South Pole have been shown by measurements of their infrared irradiances to change with the day-to-day solar wind input to the global atmospheric electric circuit, as well as to the inputs of global thunderstorms and magnetic storms. These cloud changes appear to be the cause of surface pressure changes in the Arctic and Antarctic that have long been observed to correlate with the solar wind sector structure. We analyze large data sets of cloud irradiances and surface pressures, and find differences in the responses to 2, 4, or more sectors per 27-day solar rotation. There are seasonal variations, with sign reversal in the summer, which we interpret as due to changing geometry of solar insolation input. The correlation coefficients that were shown to be statistically significant at near the 95% confidence level for all-year, all sector types show further increases for just winter months and for just 2-sector intervals. The phase relationship of the pressure responses compared to those of the cloud responses are consistent but not understood. There are also interannual variations, whose cause has yet to be determined. A parameterization of the potential distribution near the magnetic poles and out through the high latitude ionospheric region affected by solar wind inputs has been made. The daily average values depend mainly on the solar wind (interplanetary) magnetic field (IMF) B_y component, with lesser influence of the solar wind speed and IMF B_z. The correlations of IR irradiance and pressure with these parameterizations are slightly stronger than with those for the IMF B_y alone. The effects analyzed are an indication of more extensive influences of global atmospheric electricity on cloud microphysics and cloud development, which can occur on longer time scales.

1. Introduction

The electrical structure of the solar wind is highly variable, on day-to-day and long timescales, as is the physical nature and occurrence frequency of cloud cover. Thus, it is very difficult to investigate reported small effects of the solar wind on cloud properties and atmospheric dynamics, especially in the context of the hypothesized connection through the global atmospheric electric circuit and through slow acting microphysical electrical processes with time scales of days; all very difficult to obtain reliable data on at cloud level. A detailed investigation of what regularities can be seen in data sets of several decades of solar wind, cloud, and atmospheric pressure observations appears to be capable of giving insight into the mechanisms that may be involved, although the small signal/noise ratio on the day-today timescale makes analysis of subsets of the data difficult. Examples of publications dealing with day-to-day responses to the solar wind include Wilcox et al., 1973; Mansurov et al. (1974); Tinsley and Heelis (1993); Burns et al. (2007, 2008); Lam et al. (2013, 2014); Frederick et al. (2019). The amplitude of the temperature changes related to the cloud opacity changes is of order 0.3K (Frederick et al., 2019) and the surface pressure changes of order 1 hPa (Burns et al. (2007).

The global atmospheric electric circuit is bounded by the earth's surface and the highly conducting ionosphere, but the ionosphere is the lower boundary of the magnetosphere, and these do not entirely shield the middle and lower atmosphere from the highly conductive and electrically active solar wind. Inside the auroral ovals the near-vertical magnetic field lines connect to the solar wind and transmit electrical potentials generated by the solar wind Lorentz **V**x**B** electric fields to the Arctic and Antarctic polar cap ionospheres, where **V** is the solar wind speed, and **B** is the interplanetary magnetic field (IMF), and the cross product gives an electric field perpendicular to both. The east-west, or B_y, component of the IMF gives an electric field which is positive from south to north. The ionospheric potential within about 5° of the south geomagnetic pole is increased depending on B_y, by 20kV or so on average, while depressed near the north geomagnetic pole by about the same amount (e.g., Tinsley and Heelis, 1993, Lam et al, 2013). There are also potentials on the dawn and dusk side of the auroral ovals generated by solar-wind-induced field aligned magnetospheric currents. The solar wind (or interplanetary, IMF) magnetic field, and thus its B_y component and the ionospheric potential inputs, reverse frequently, at times twice or four or more times per 27-day solar rotation, creating the sector structure as observed by Ness and Wilcox (1965), with corresponding reversals of the B_y input to the polar cap ionospheres. Daily average values of B_y are available at the NASA/GSFC web site (NASA, 2018). Based on the B_y variations, the time series can be divided into intervals which we treat as 2-sector, 4-sector, or variable (irregular or more than 4) sector intervals. Figure 1 shows four years of variations of B_y as well as of B_z (the north-south IMF component) and the solar wind speed, from the NASA/GSFC web site, and examples of our characterizations.

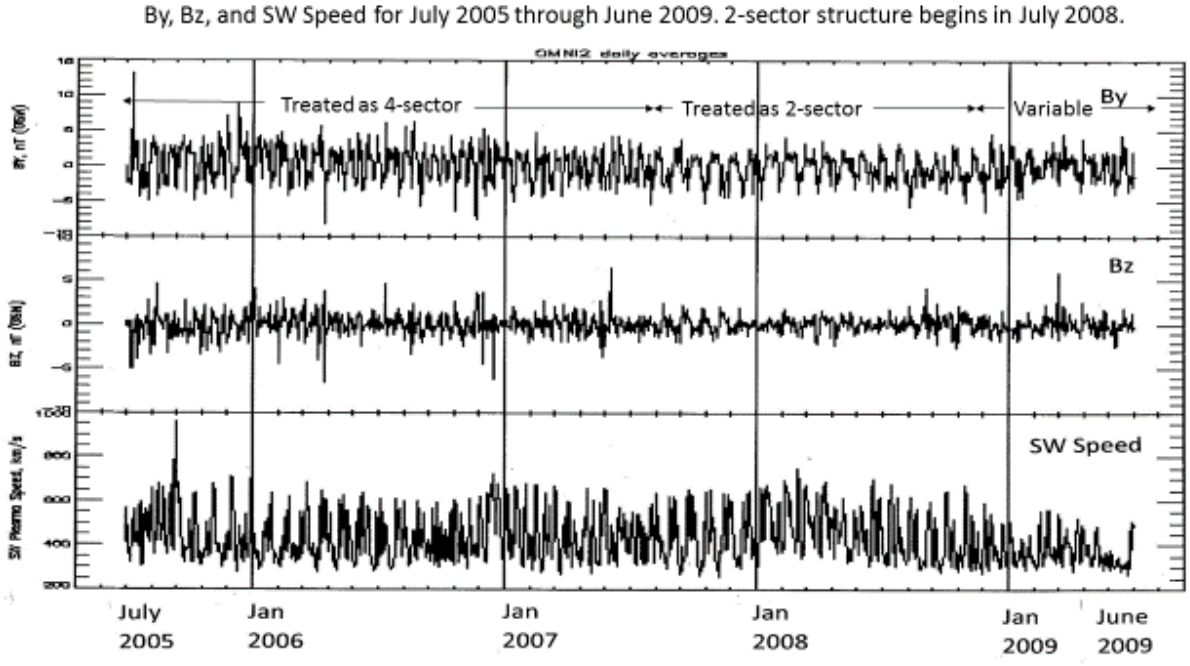

Figure 1. Time series of IMF B_y (top panel), IMF B_z (middle panel) and solar wind speed (lower panel) July 2005 to June 2009, from NASA (2018). Intervals of sector structure are designated 2-sector, 4-sector or variable (irregular or more than 4 sectors).

The solar wind-induced polar ionospheric potential changes are superimposed on an otherwise nearly globally uniform but time-varying ionospheric potential, generated by thunderstorms and highly electrified convective clouds at low latitudes (e.g. Hays and Roble 1979, Roble and Hays, 1979). These

meteorological generators send a total of about 1000 Amperes to the ionosphere and charge it electrically to a potential of about 250kV. All over the globe this potential difference between the ionosphere and the surface drives a downward current density of order a few pA/m^2, and as if flows through clouds it alters the amount of electric charge that would otherwise be on droplets and aerosol particles due to ionization by galactic cosmic rays. The current density, at a given location and in the absence of changes in atmospheric aerosol and in the cosmic ray flux, is proportional to the overhead ionospheric potential (Tinsley, 2008). Measured vertical electric field values at ground level, which are proportional to current density, made close to the southern magnetic pole at Vostok, show the expected changes as B_y changes at sector boundaries (Burns et al., 2006, Figs. 2 and 3).

Figure 2 shows diagrams of northern hemisphere dawn-dusk section of the global circuit. The top panel is from Markson (1983), showing the low latitude convective cloud generators and the high dawn and low dusk potentials near the auroral zone that are due to magnetospheric currents driven by IMF B_z. The lower panel is from Tinsley and Heelis (1993) showing the reduction of ionospheric potential within the northern auroral zone due to positive IMF B_y, and the increase there due to negative B_y. The average of the potential distribution over the area of the polar cap, and over time, varies most strongly with IMF B_y, as determined by the sector structure, except during magnetic storms.

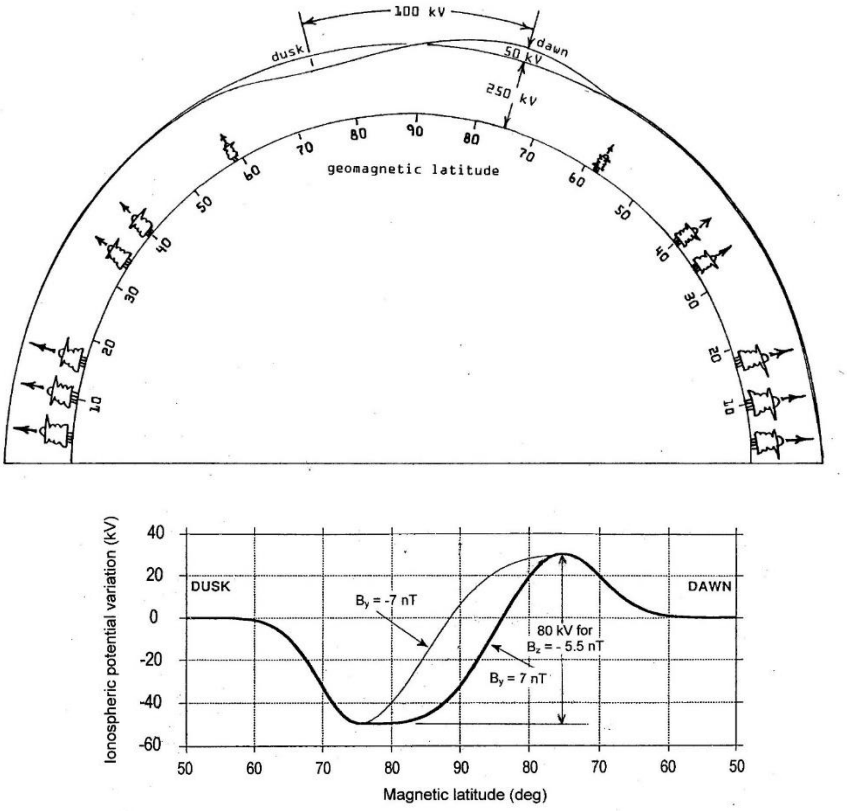

Figure 2. Diagrams of East-West sections through the northern hemisphere of the global electric circuit, top: from Markson, (1983) showing the dawn and dusk ionospheric potential changes induced by IMF B_z, and bottom; from Tinsley and Heelis, (1993) the potential changes induced by IMF B_y.

There is theory and evidence, reviewed by Lam and Tinsley, (2016) that the changes in the downward current density (J_z) in the global circuit have small effects on the electric charges on, and the collision rates of, droplets and aerosol particles. These can affect microphysical processes in clouds, and cloud development, but such effects are difficult to distinguish from all the other inputs that contribute to variability in clouds. Fortunately, the variable solar wind components have been observed for more than 50 years, and the B_y input, with its reversals two or more times per month, offers a sufficiently long time series for correlations with meteorological parameters to separate out the effects of atmospheric electricity from those of the many other inputs into the weather and climate system. The polar cap B_y - related potential variations are only 20% or so of the total ionospheric potential, and cover only about 1% of the globe, but the stratus-type clouds in polar areas persist for days, allowing time for small changes in the microphysics that affect condensation nuclei and ice production to accumulate. The clouds are often of optical thickness less than unity, and so that they are particularly sensitive to changes in their microphysics that can affect their optical thickness and their radiative coupling to the atmosphere (Mauritsen et al., 2011).

Alert, Canada is about 3° from the north geomagnetic pole, and continuous observations of downwelling and upwelling infrared irradiance have been made there since 2004, and are available at the NOAA web site (NOAA 2018). It was shown by Frederick et al. (2019) that the daily average irradiances 2004-2015 showed statistically significant correlations with the IMF B_y component, with a lag of 3 or 4 days, and an amplitude equivalent to cloud and surface temperature changes of about 0.3° C. This lag of several days raises the question of how the surface pressure variations are related to the cloud opacity variations. Such relationships between cloud opacity and cloud radiative forcing are expected (Ramanathan et al., 1995), but the clouds and the atmosphere have their own internal dynamics, which can affect phasing of the coupling of periodic variations.

In this paper we examine how the phase relationships to the solar wind sector structure, of both the irradiance and surface pressure, vary through the seasons, as a clue to their relationships to each other. We examine how the amplitude of the responses change with the number of sectors per solar rotation. We look at interannual variations of the pressure response since 1995, for evidence of solar cycle effects on the solar wind input, and for possible effects of changing atmospheric aerosol concentrations. The hypothesized mechanism involves electric charge effects on scavenging of aerosol particles by droplets, and so would be expected to be sensitive to aerosol concentrations changes.

2. Observations at Alert of irradiance variations

The daily average infrared irradiances at Alert have an annual variation with a maximum in summer, as illustrated by Frederick et al. (2019). To examine correlations and for use in superposed epoch analyses with respect to the solar wind input the daily values of the downwelling and upwelling infrared irradiances were smoothed with a running mean, covering 13 days before and after the central day, but excluding that day, and the differences of the observed values from the running means evaluated. Figure 3 is of a time series of the correlations between the differences for the upwelling radiance (U_IR) and the differences for the downwelling irradiances (D_IR) in a running 27-day window. The time series runs from 2004 to 2015. The correlation coefficient of D_IR and U_IR is around 0.8 in the winter, but decreases and becomes negative, reaching about - 0.5 in June-July of each year. This effect can be understood in terms of the optical thickness of the overhead stratus-type clouds increasing and decreasing. In the absence of sunlight in winter, thickening of clouds, whether or not due to

atmospheric electricity, reduces the escape of radiation to space, and warms both the clouds and the surface. In sunlight, however, thickening clouds cool the surface by reducing the sunlight reaching it, more than their increased thickness radiates more heat downwards. In Fig. 1 other effects may be due to melting snow cover and mid-summer convection.

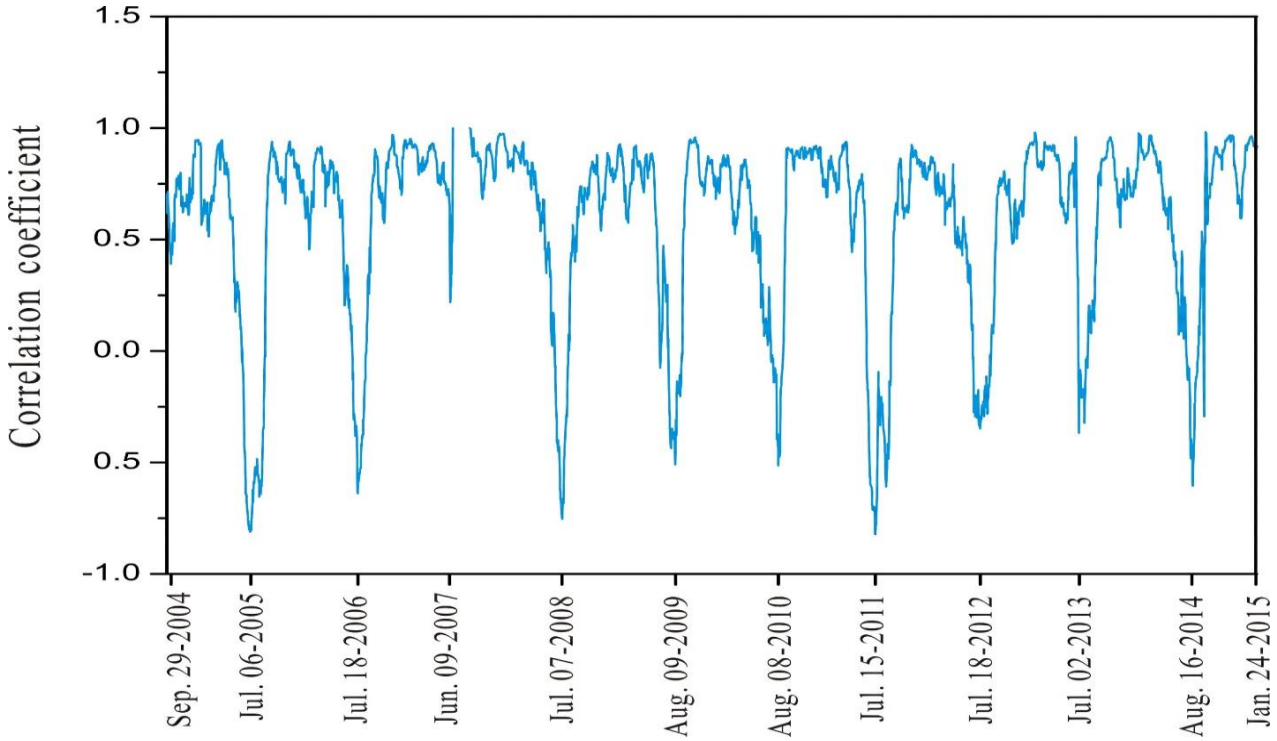

Figure 3. Correlation in a running 27-day interval between the daily mean downwelling infrared irradiance (D_IR) and the upwelling irradiance (U_IR) measured at Alert, Canada 2004-2015.

The sector structure of the solar wind can vary from 2-sector to 4 sector to multiple and irregular sector structures over intervals of a few months to a few years, as in Fig. 1. In our analyses we generally do not use intervals multiple or irregular sectors, as for these the correlation coefficients found are small and variable. A table of intervals of these sector types, designated by inspection of plots such as in Fig. 1, from 1993 to 2018, is given in Appendix A.

Because a positive excursion of IMF By produces a negative excursion of ionospheric potential in the northern polar cap and to a positive excursion in the southern polar cap, a general treatment for correlations with sector structure in both hemispheres is preferably made in parameters representing ionospheric potential. In Appendix B we show the results of fitting parameters to the model by Weimer (1996) based on satellite measurements of potential as a function of solar wind parameters. This parameterization allows us to take into account the small effects of the solar wind speed, V, and the IMF B_z component as well as the major effect of IMF B_y on both the potentials at the north and south

magnetic poles (VpN and VpS respectively), and on the area-integrated potential over the northern and southern polar caps (SigmaN and SigmaS respectively).

2.1. Correlations of Alert irradiance variations with ionospheric potential.

Figure 4 shows lagged correlations of D_IR and U_IR with negative IMF B_y and VpN, for all months and for all sector types. This is an extended and inverted version of the Figure 5 of Frederick et al (2019), and is a plot of correlation coefficient rather than regression coefficient. Frederick et al. (2019) showed that the response to B_y is significant at about the 95% level. The correlation coefficients exhibit a strong solar rotation 27-day repetition, implicit in the sector structure. The correlation coefficients with VpN have a larger range than with ($-B_y$) from negative to positive, attributable to a better representation of the overhead ionospheric potential than that of ($-B_y$). The 2004-2015 period covers 144 solar rotations. Positive lags in this and following figures are for solar wind variations leading the irradiance or pressure variations.

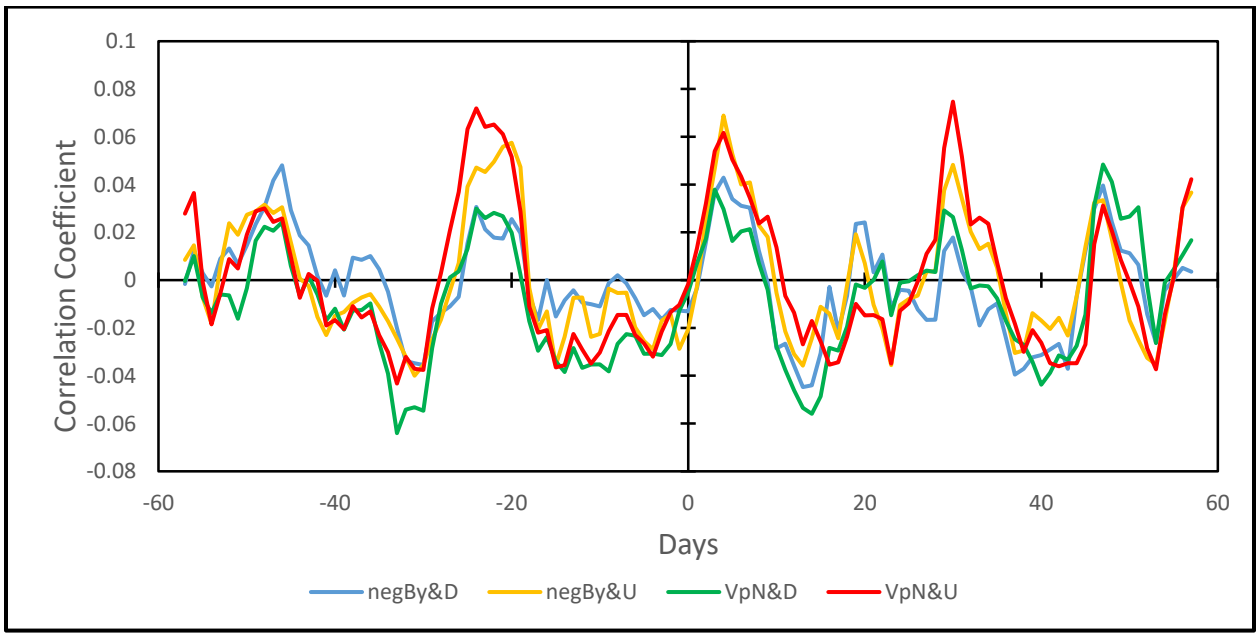

Figure 4. Lagged correlations for all seasons and all sector types of D_IR and U_IR with (-By), blue and orange curves respectively; and with VpN, green and red curves respectively, 2004-2015.

Figure 5 shows the same analysis as Fig. 4, but restricted to October through April intervals. The correlation coefficients now range up to 0.1, and there is less difference between the U_IR and D_IR curves.

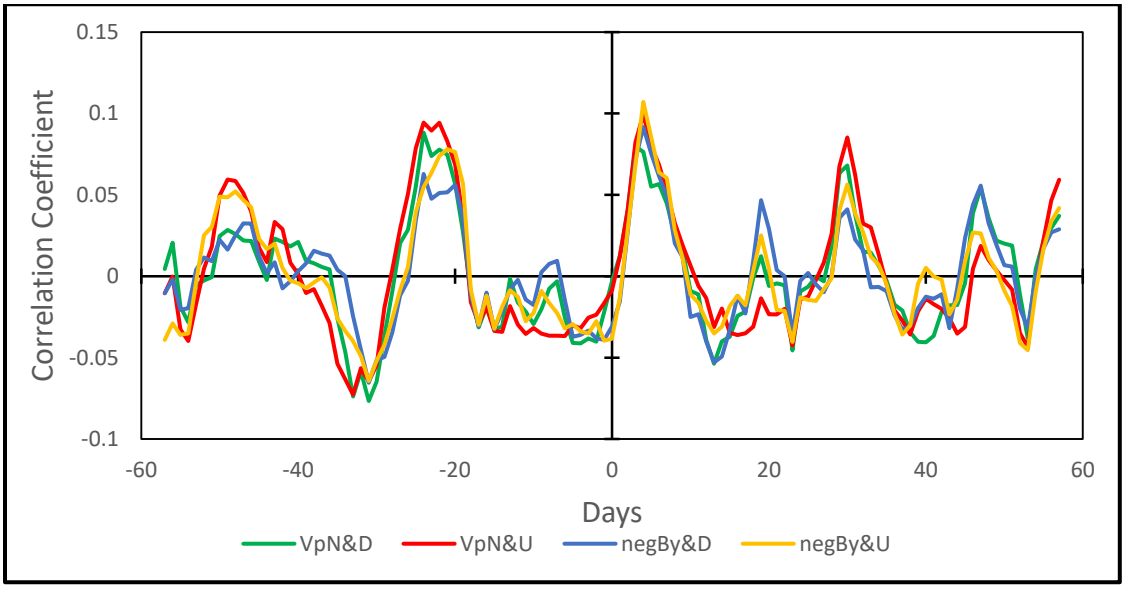

Figure 5. Lagged correlations for each October through April and all sector types of D_IR and U_IR with ($-B_y$), blue and orange curves respectively; and with VpN, green and red curves respectively, 2004-2015.

Figure 6 shows correlations of the irradiances with VpN for combined 2 and 4-sector intervals only, for October through April intervals of D_IR (green) and U_IR (red); also for each May-June with D_IR (grey) and U_IR (yellow). For October-April intervals, the results are similar to those of Figure 5 with variable and irregular intervals of solar wind structure included, but for May-June the results for U_IR are of opposite phase to those for October-April; of larger amplitude, and opposite to those for U_IR. This is consistent with the results of Fig. 3, and shows that the upwelling irradiance, representing surface temperature and influencing surface pressure, and not the downwelling irradiance, is most affected for these months. These effects will become clearer in the later analysis of surface pressure over the much longer 23-year interval.

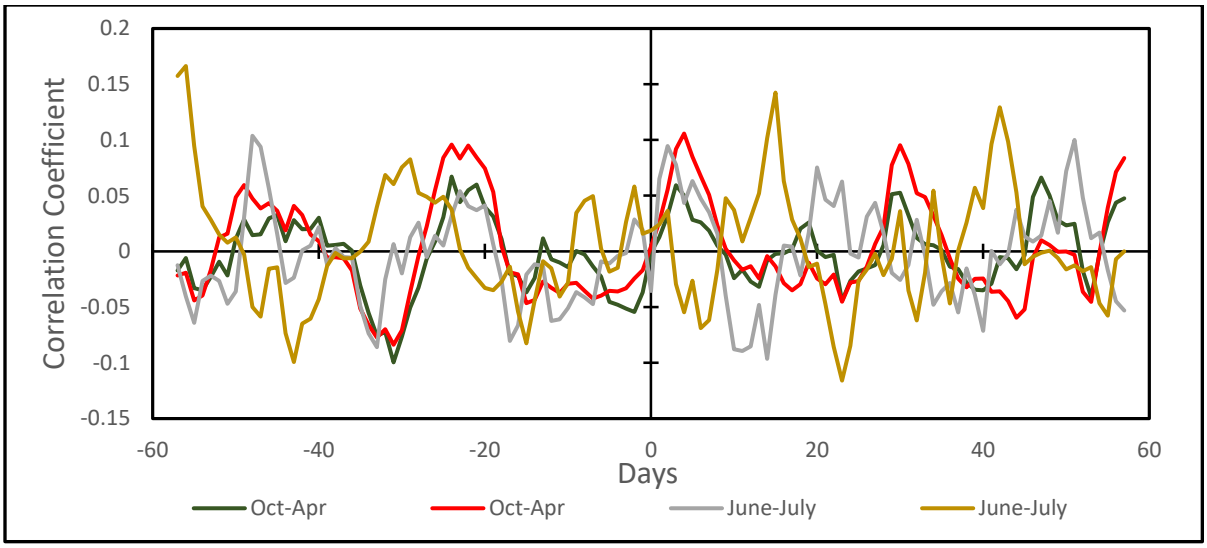

Figure 6. Lagged correlations with VpN for each October through April of D_IR (blue) and U_IR (red); also for each May-June with D_IR (grey) and U_IR (yellow); for combined 2 & 4 sector solar wind intervals, 2004-2015.

Figure 7 shows lagged correlations of only 2-sector U_IR values with VpN for October-April months during 2007-2008 (orange) and during 2010-2015 (blue) with the overall correlation in black. They are of larger amplitude, reaching a correlation coefficient of 0.2, than the correlations for combined 2 & 4 sector segments, partly because successive 4-sector segments occur at a variable spacing within repeating 27-day periods structures. In view of the lag time for the responses, it may also be because each 2-sector variation lasts twice as long as a 4-sector variations, this allows a greater response to develop. The correlations are a little stronger for the solar minimum period 2007-2008.

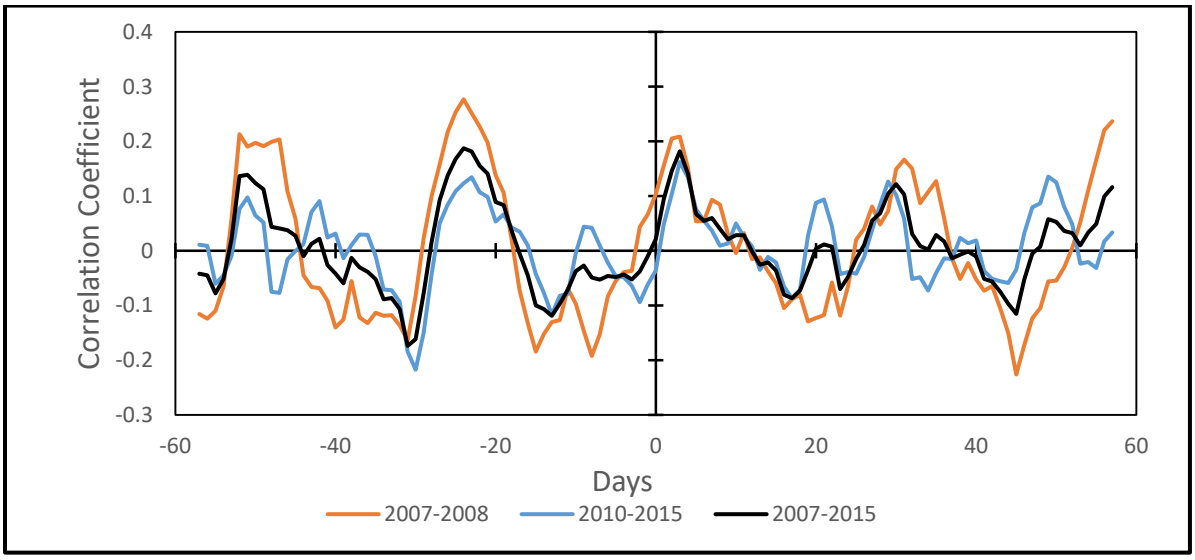

Figure 7. Lagged correlations of 2-sector U_IR values with VpN for October-April intervals: Oct 1 2007-to Nov 17 2008 (orange); Jan 11 2010 - Feb 22 2015 (blue): Overall correlation, (black).

2.2. Correlations for irradiances across sector boundary types

The previous analyses of correlations do not show possible differences in the cloud response to increases in ionospheric potential as opposed to decreases in ionospheric potential. So the data were stratified into 14-day portions, centered on either a negative to positive sector boundary, or a positive to negative sector boundary. The VpN values, for averages of the 7 days before or after the SBC, were extended for a further 7 days before or after, so that a lagged correlation could be made over the 7 days before or after zero lag. The shortened winter period of October-March is used to focus more on the cold season and minimal sunlight extending to lower latitudes. Figure 8 shows the result for positive to negative SBCs, for combined 2&4 sectors, for D_IR (grey) and U_IR (yellow), and for just 2-sectors for D_IR (orange) and U_IR (green).

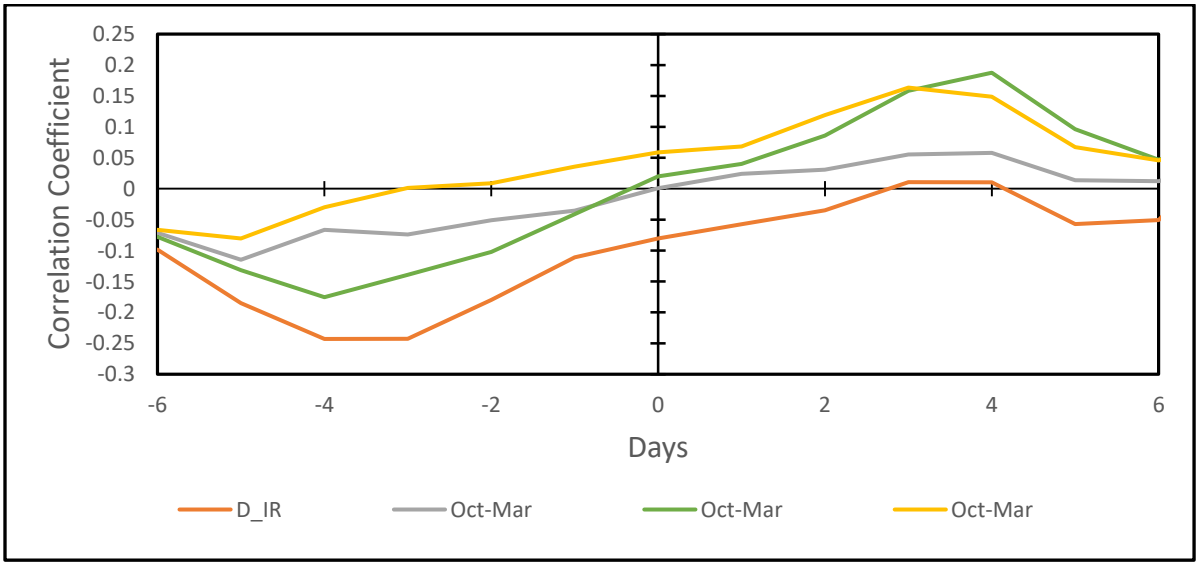

Figure 8. Lagged correlation with VpN for isolated -7d to +7d portions of +to- sectors of Alert irradiance data, 2004-2015. For October-March intervals for the combined 2&4 sectors, D_IR (grey) and U_IR (yellow); and for just 2-sectors, D_IR (orange) and U_IR (green).

Figure 9 shows the corresponding result for negative to positive SBCs, for combined 2&4 sectors, for D_IR (grey) and U_IR (yellow), and for just 2-sectors for D_IR (orange) and U_IR (green). There is a general similarity with the correlations across the negative to positive sectors in Fig. 8, with again a larger amplitude of change for the 2-sector crossings than for the combined 2&4 sector crossings. The peak correlation for lags of about 3 or 4 days in Fig 8 compares with peaks at about 2 days lag in Fig 9, but this difference could be an effect of noise, i.e., unrelated day to day variations in the data.

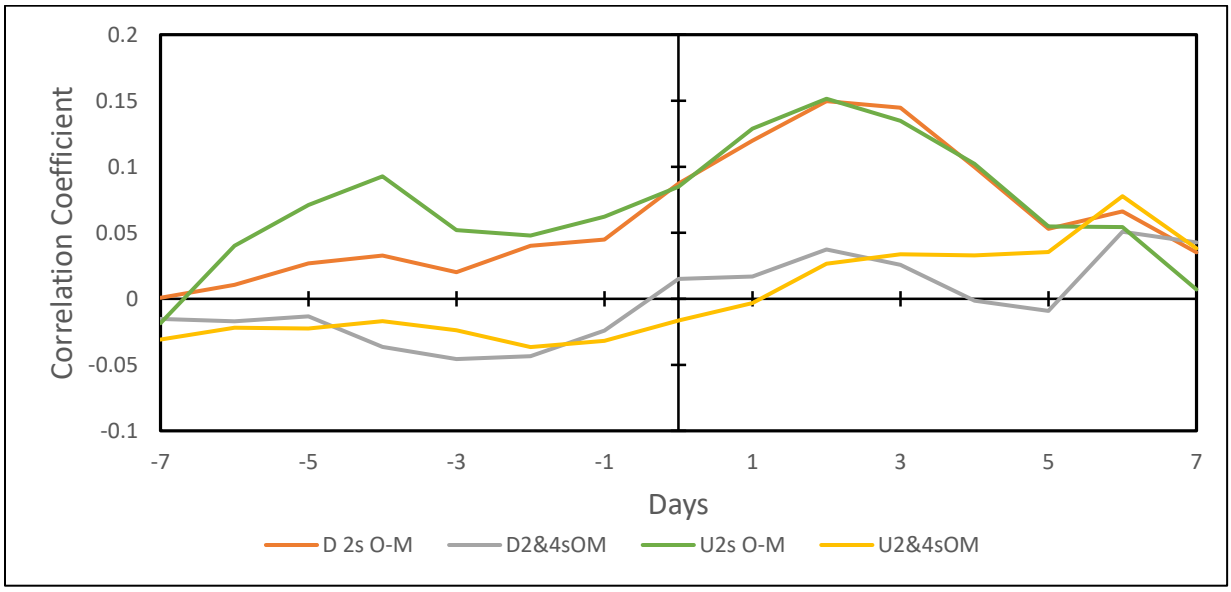

Figure 9. Lagged correlation with VpN for isolated -7d to +7d portions of –to+ sectors of Alert irradiance data, 2004-2015. For October-March intervals for the combined 2&4 sectors, D_IR (grey) and U_IR (yellow); and for just 2-sectors, D_IR (orange) and U_IR (green).

2.3. Superposed epoch irradiance analysis

The times at which By changes sign define the sector structure, and are known as sector boundaries. We can make superposed epoch analyses of irradiance or pressure across these sector boundaries. From our time series of By or VpN or SigmaN we identified these boundaries, and separated the positive-to-negative boundaries in ionospheric potential from the negative-to-positive ones. We utilized boundaries

with at least 5 days of one sign of VpN before the crossing, and 5 days afterwards. The number of data points going into the averages for each day before or after the boundary is greatly reduced from the set of all the data points generating each point on the lagged correlation analyses, and so the noise level are correspondingly increased, and the statistical significances reduced. Nevertheless, we show in the following figures superposed epoch analyses for the available data. To clarify the trends the results in the figure has been smoothed with a (1:2:1)/4 running mean.

Figure 10 shows superposed epochs of irradiances for Alert for + to – sector boundary crossings. There were 28 crossings in 2004-2014 satisfying the criteria for sector stability. The standard errors of the mean average 4.2 units for D_IR and 3.6 units for U_IR. Thus the changes across the boundary are significant at better than 95%. The units of irradiance are W/m^2. For the ionospheric potential change, 10 units of VpN/3 correspond to 30 kV. At a mean cloud temperature of 256K, 10 W/m^2 corresponds to a change in temperature of 2.6K.

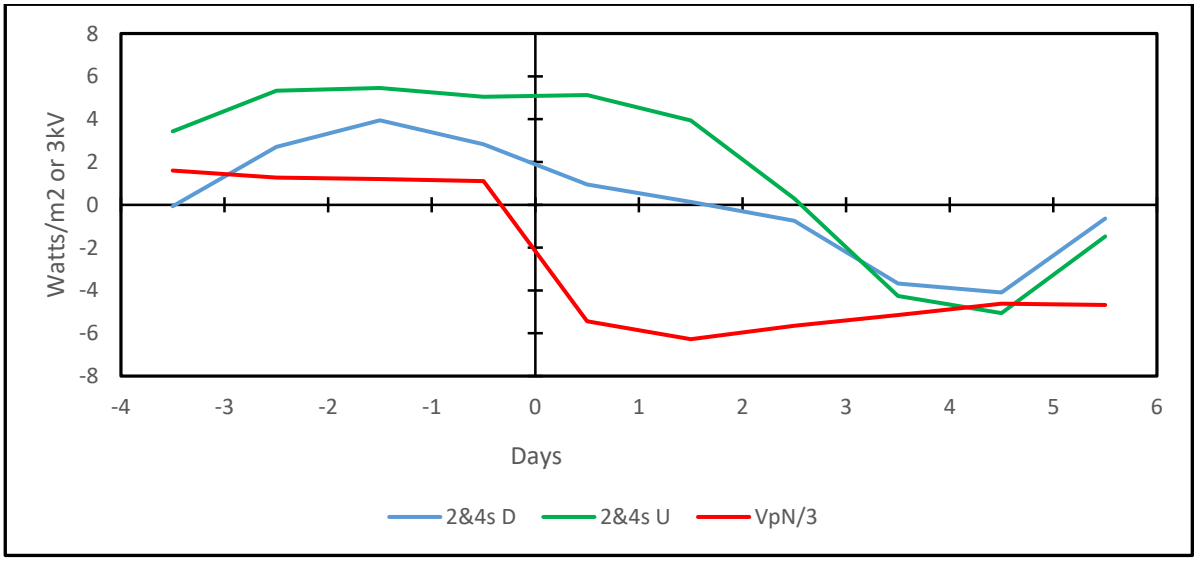

Figure 10. Superposed epoch analyses of changes in Alert irradiances and VpN across 2&4, + to -, sector boundaries. D_IR (blue) and U_IR (green) can be compared to VpN/3 (red). Data for October - March, 2004-2015. The units of irradiance are W/m^2. Ten units of VpN/3 correspond to 30 kV of the ionospheric potential change.

Figure 11 shows superposed epochs of irradiances for Alert for - to + sector boundary crossings. There were 47 crossing in 2004-2014 satisfying the criteria for sector stability. The units are the same as for Fig. 10.

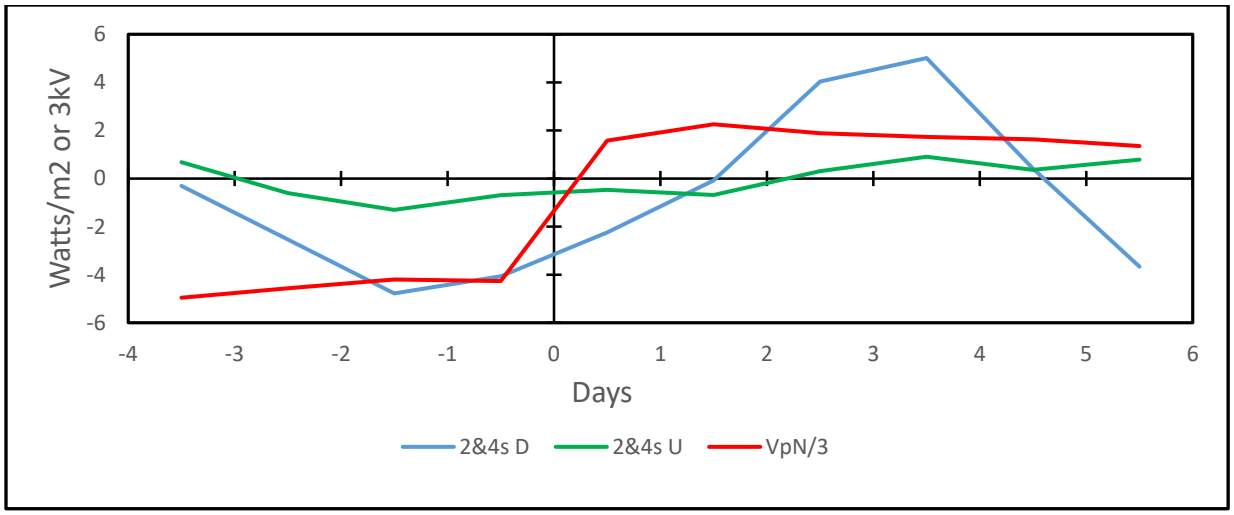

Figure 11. Superposed epoch analyses of changes in Alert irradiance and VpN across 2&4 sector, – to + sector boundaries. D_IR (blue) and U_IR (green) can be compared to VpN/3 (red). Data for October - March, 2004-2015. The units of irradiance are W/m^2. Ten units of VpN/3 correspond to 30 kV of the ionospheric potential change

The results of both Figs 10 and 11 are consistent with the lags of 2 to 4 days found in the correlation analyses for the response of the irradiances to the change in overhead ionospheric potential. The standard errors of the mean are 3.5 W/m^2 for D_IR and 2.5 W/m^2 for U_IR. The results for D_IR are statistically significant at the 95% level, but those for U_IR are not. It is expected that the uncertainties will be reduced when the more recent five or more years of irradiance data are available.

3. Observations of surface pressure responses

A much longer time series (compared to that for irradiance data) of surface pressure reanalysis data (Kalnay et al., 1996; NOAA/NCEP 2018) is available for analyzing responses to the solar wind (and to atmospheric electrical inputs) of atmospheric dynamics at high and mid-latitudes. The solar wind affects ionospheric potential and the current density down through clouds within about 5° (~600 km) of the magnetic poles, and zonal atmospheric winds, combined with the lifetime of days for the clouds, and the ability to reduce noise by averaging over larger areas, suggests zonal mean pressures be used instead of grid-point pressures for evaluating amplitudes and lags of responses for seasonal, interannual, and sector length related variations. The zonal averages of pressure for each zone of 2.5° latitude were weighted by the area of the zone and summed for broader bands

3.1. Correlation of bands of zonal pressure with ionospheric potential

Figure 12 shows lagged correlations for the pressure band 81°-71°N. These are for 2 & 4 combined solar wind sector intervals, for October-March, with curves for each of (-By) (blue), VpN (orange) and SigmaN (grey). As with the irradiance data, the correlations are stronger with VpN (and SigmaN) than with ($-B_y$). A noteworthy result is that the correlations, if positive, peak about 2 days earlier than zero lag, and thus about 5 days earlier than the irradiance variations. The implications of this result are postponed for later discussion.

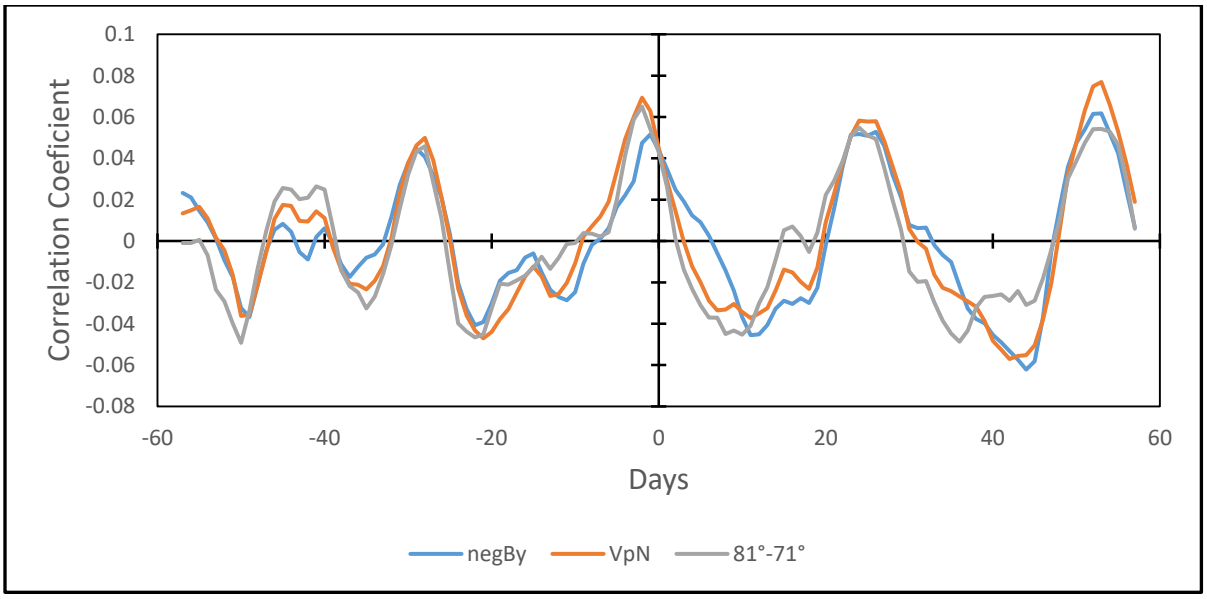

Figure 12. Lagged correlations of surface pressure 81°-71°N in the same format as Fig 4 with ($-B_y$) (blue); VpN (orange); and SigmaN (grey), for October-March intervals 1995-2018. Only the 2 & 4-sector intervals of solar wind structure were used.

Figure 13 compares the correlations in the summer months of June-July, for the latitude range 81°-71°N, for 2 & 4 combined solar wind sector intervals, with the correlations for October-March. The pressure variations for the summer months have out of phase and negative correlations with the solar wind input, compared to those for October-March, and have a range exceeding those for October-March. This result is similar, but phase shifted, compared to that for the longwave upward irradiance variations (Fig 6) which have poorer signal/noise.

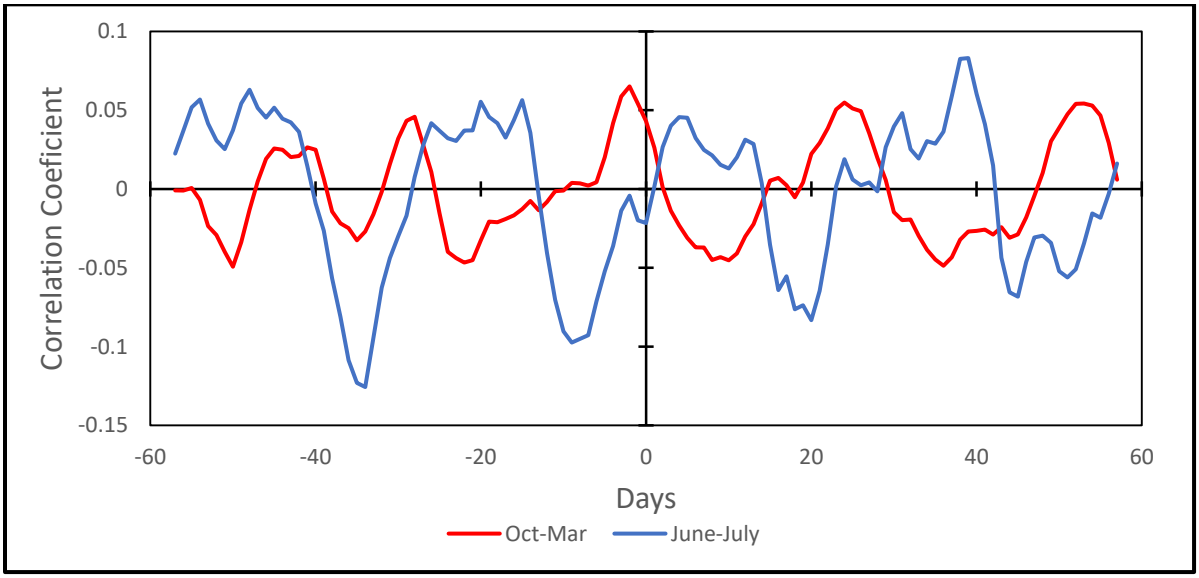

Figure 13. Lagged correlation of the zonal mean pressure 81°-71°N with SigmaN for 2&4 sector intervals, October-March (red); June-July (blue).

Figure 14 is for the 20° wide latitude band 90°N to 71°N to further reduce the noise, for October-March months, for lagged correlations of pressure with SigmaN. The data for 4-sector intervals have been

separated from those for 2-sectors intervals. The 13-day periodicity of the response for 4-sector intervals compares to the 27-day periodicity for the 2-sector intervals.

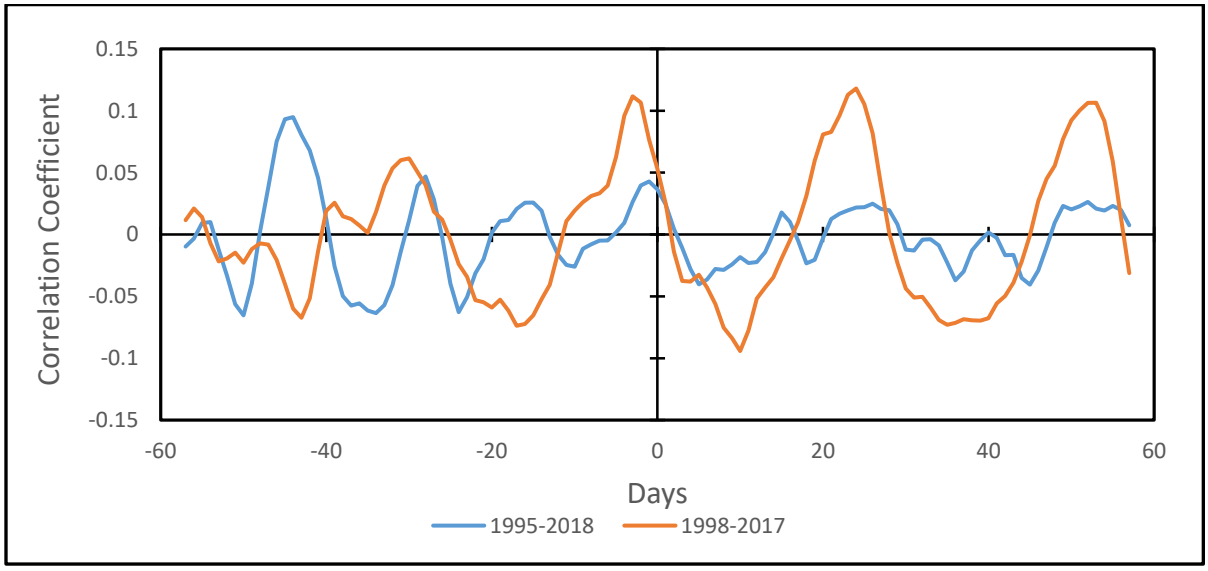

Figure 14. Lagged correlations for the band from 90°N to 71°N with SigmaN, with the data for pressure responses to 4-sector intervals (blue) separated from those to 2-sectors (orange). Oct-March intervals, 1995-2018.

Figure 15 compares lagged correlations of pressures in three 10° wide latitude bands with SigmaN. The results are for October-March for 2&4 solar wind sector intervals 1995-2018. Those for 90°-81°N and 81°-71°N latitudes are similar, and that for 41°N-31°N is opposite, consistent with earlier work (Lam et al., 2013; Zhou et al., 2018) and the principle that the total weight of the Earth's atmosphere must remain constant. The previously published results for the latitude variations were for zero lag. The results here show the zero lag values are of reduced amplitude compared to the peak values at lag about -2d. The results for latitudes between 71°N and 41°N are intermediate between the higher and lower latitude results and have lower correlation coefficients.

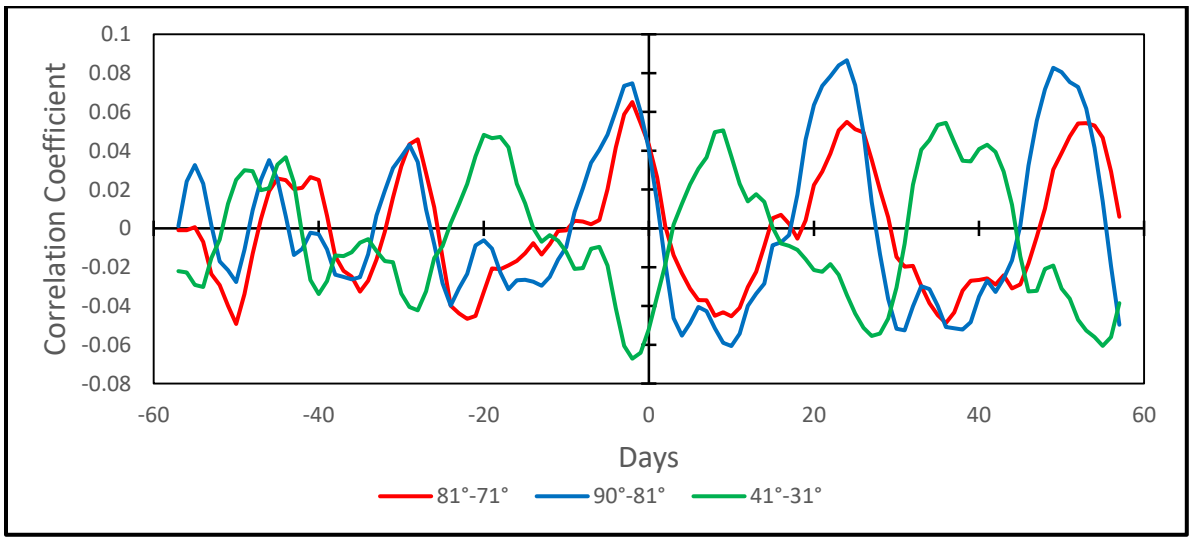

Figure 15. Comparison of lagged correlations with SigmaN for 2&4 solar wind sectors in three 10° wide latitude bands for October-March intervals. 90°-81°N (blue); 81°-71°N (red); 41°-31°N (green). 1995-2018.

Figure 16 shows lagged correlations for pressure in the band 90°-71°N for 2-sector solar wind structures in October-March months with VpN. The interval 1998-2017 is split into three sections that include all 2-sector data; 1998-2004, 2007-2015, 2015-2017. There is a considerable increase in the correlation coefficient in 2015-2017 compared to the other two intervals, and changes in the lag between all three. The VpN (and By and SigmaN) excursions in 2015-2017 were less than in the other two intervals, so the larger pressure amplitude, corresponding to about 2.4 hPa from minimum to maximum, cannot be attributed to a stronger solar wind driver. The implications of this result are postponed for later discussion.

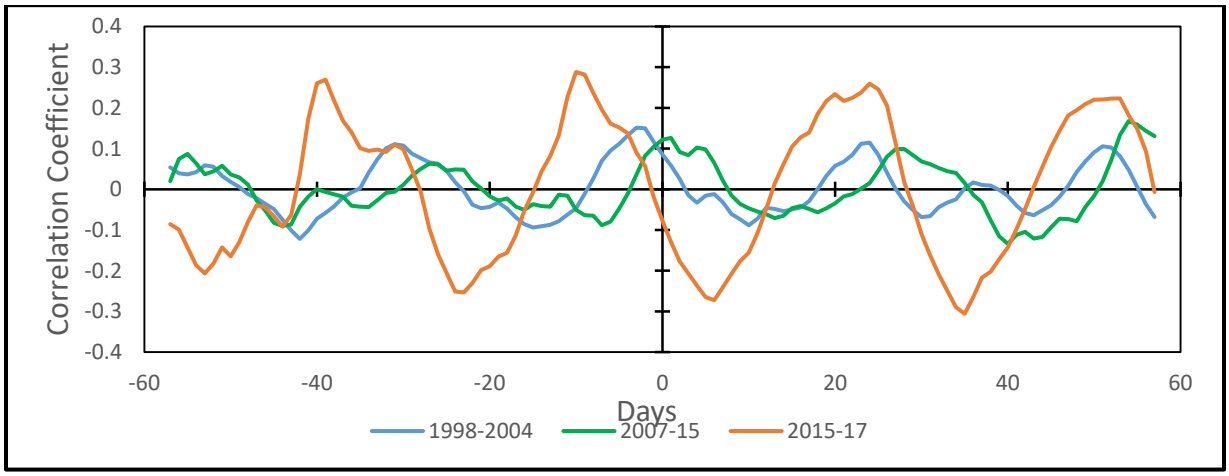

Figure 16. Lagged correlation of pressure band 90°-71°N with SigmaN, for 2-sector October-March intervals. December 1998 - March 2004 (blue); October 2007 - February 2015 (green); October 2015 - March 2017 (orange).

3.2 Correlations for pressure across sector boundary types

As with the irradiance data, we separated the pressure data into 14-day intervals, centered on sector boundaries with either positive-to-negative VpN transitions, or on negative-to-positive transitions. The VpN values were extended for a further 7 days before or after, so that lagged correlations could be made for lags of -7d to + 7d. Figure 17 shows the result for the positive-to-negative transitions for latitude ranges of 90°-71°N and 51°-31°N. For 90°-71°N the region of positive correlation extends with approximately constant amplitude from lags of -3d to +1d, for both 2-sector and 4-sector intervals. For 51°-31°N there are minima varying from -3d for the 4-setor case to +1d for the 2-sector case.

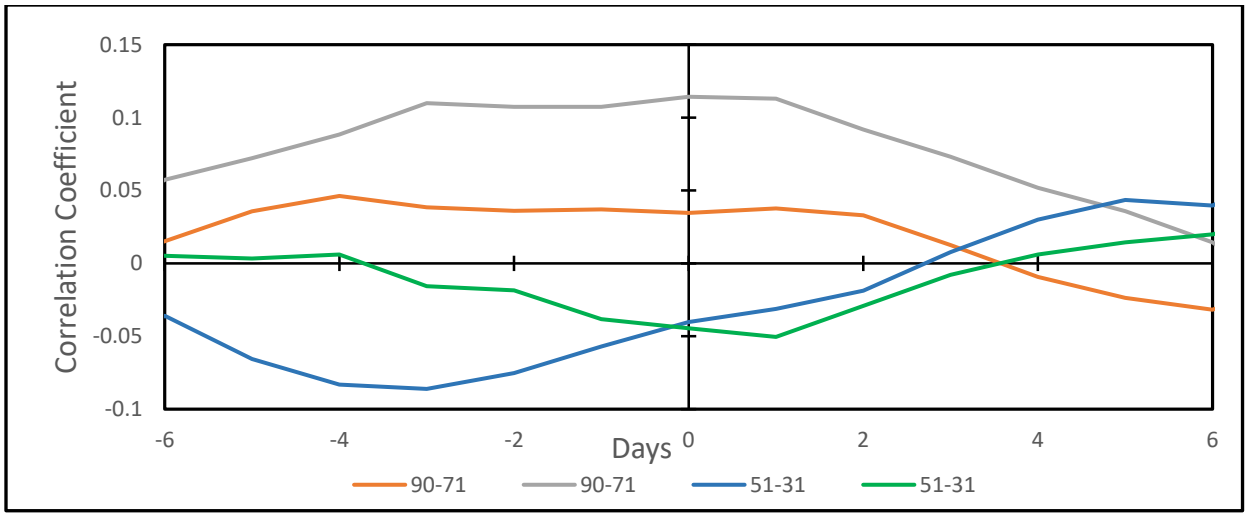

Figure 17. Lagged correlations for isolated -7d to+7d portions of + to - sectors, 2005-2018. For 90°-71°N 2-sector (grey) and 4-sector (orange). For 51°-31°N 2-sector (green) and 4-sector (blue).

Figure 18 is the corresponding set of curves for negative-to-positive VpN transitions for sector boundaries. Here the maxima of the 90°-71°N curves are at lags of -3d and 2d, while the 51°-31°N curves have minima from -7d to -1d, and prominent maxima at +3d to +6d. While in both Fig 17 and Fig 18 the lower latitude variations are generally opposite to the high latitude variations, there are differences that may be attributable to processes considered in the Discussion section.

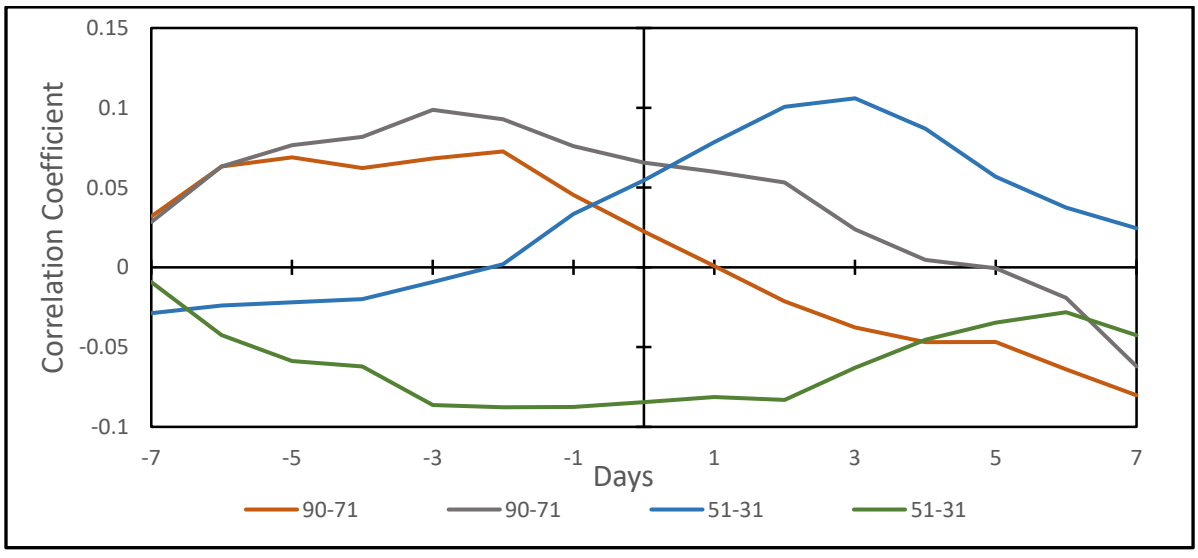

Figure 18. Lagged correlations for isolated -7d to +7d portion of - to + sectors, 1995-2018. . For 90°-71°N 2-sector (grey) and 4-sector (orange). For 51°-31°N 2-sector (green) and 4-sector (blue).

3.3. Superposed epoch pressure analysis

Figure 19 shows a superposed epoch analysis of the products of pressure times band area in the 20° wide bands 90°-71°N and 51°-31°N for the months October-March in 1995-2018. These are + to – changes in the north polar cap ionospheric potential. Also shown is the superposed epoch result for VpN/2 (moved up by 2 units for clarity). We show the 4 with 2 segment intervals (4s&2s) as well as the 2s intervals, with the latter having the larger amplitude. The lower latitude 51°-31°N result changes in the opposite sense to the high latitude 90°-71°N result, as found in the correlation analysis. There were 110 crossings in 2004-2014 satisfying the criteria for sector stability. As fractions of the surface area of the northern hemisphere, the pressure band 90°-71°N is 0.053, and that of the band 51°-31°N is 0.261. Pressure-area units are Pascals multiplied by the fractional surface area of the band, so 10 units on the plots correspond to 10/.053 = 188 Pa or 1.9 hPa for the 90°-71°N band, and 10/.261 = 38Pa, or 0.4hPa for the 51°-31°N band. The standard errors of the mean for 90°-71°N are 2.7 and 4.0 units for 2s&4s and 2s curves respectively. Standard errors of the mean for 51°N-41°N are 4.0 and 7.5 units for 4s&2s and 2s curves respectively. The changes across the sector boundaries are better than 90% statistically significant. To clarify the trends the results in the figures have been smoothed with a (1:2:1)/4 running mean.

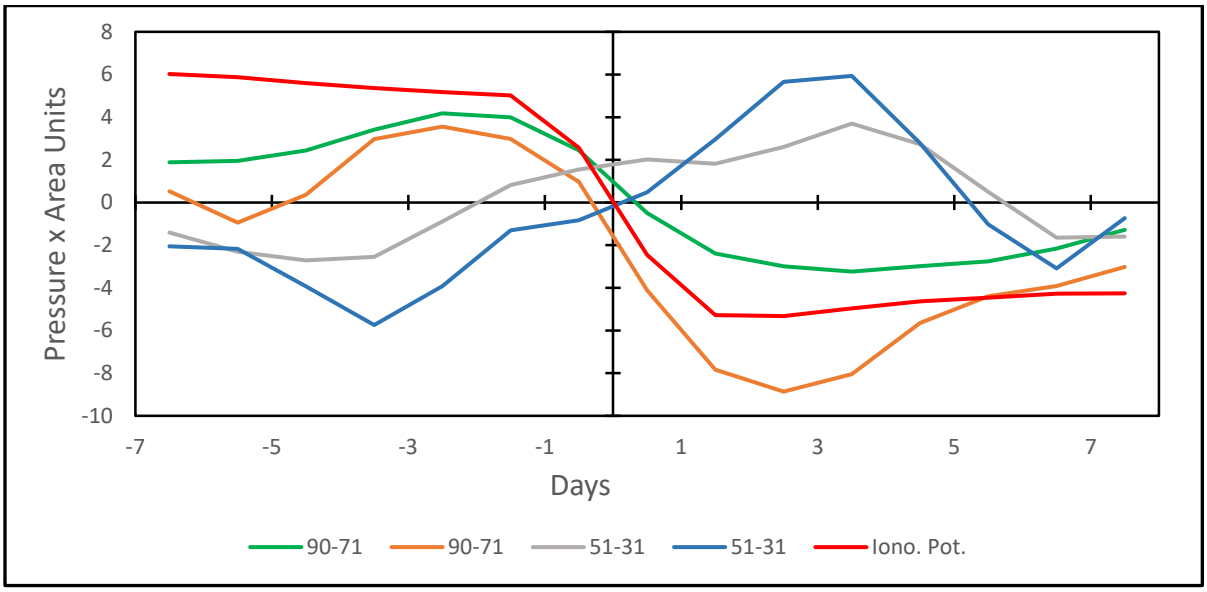

Figure 19. Superposed epoch analysis of pressures 90°-71°N 2s&4s (green), 2s (orange); 51°-31°N 2s&4s (grey), 2s (blue) across sector boundaries for + to – VpN changes; also of (VpN/2+2) (red). October-March, 1995-2018. Ten units of VpN/2 correspond to 20 kV of ionospheric potential change. For the pressure·area values, 10 units on the plots corresponds to about 2 hPa for the 90°-71°N band, and about 0.4hPa for the 51°-31°N band.

Figure 20 is as for Figure 19 except that it is for – to + changes in the northern polar cap ionospheric potential. For high latitudes the pressure change is also positive to negative. Again the 2s intervals have the larger amplitude, and the lower latitude 51°-31°N result changes in the opposite sense to the high latitude 90°-71°N result, as found in the correlation analysis. There were 110 crossings in 2004-2014 satisfying the criteria for sector stability. Standard errors of the mean 90°-71°N are 2.5 and 3.5 units for 2s&4s and 2s curves respectively. Standard errors of the mean for 51°N-41°N are 3.5 and 5.5 units for

4s&2s and 2s curves respectively. Thus the changes across the sector boundaries are better than 95% statistically significant.

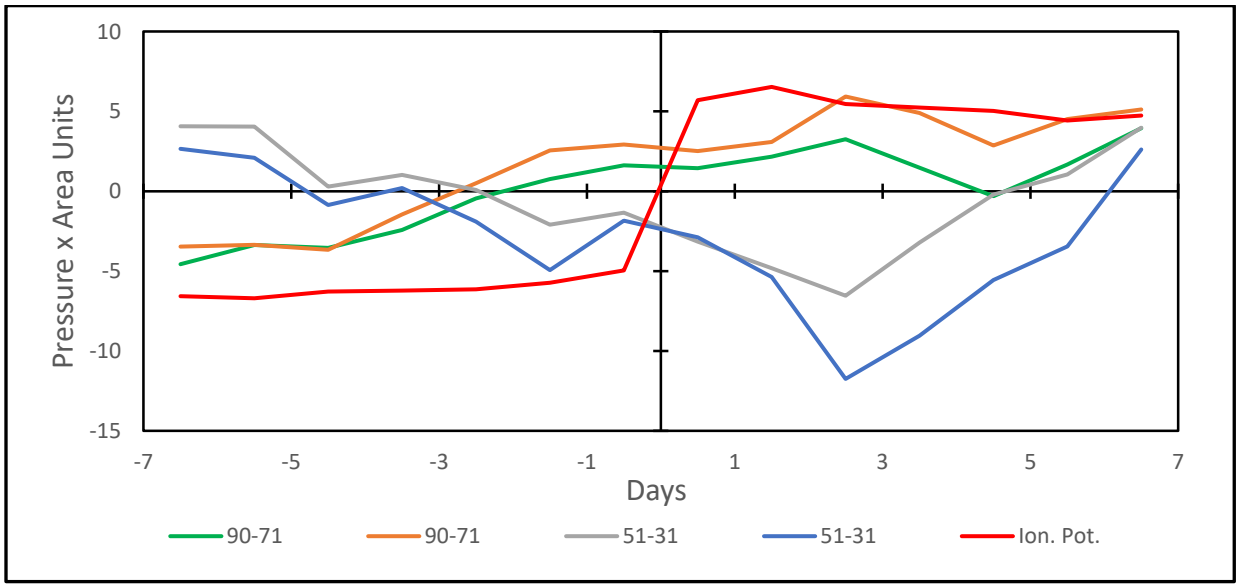

Figure 20. Superposed epoch analysis of pressures 90°-71°N 2s&4s (green), 2s (orange); 51°-31°N 2s&4s (grey), 2s (blue) across sector boundaries for + to - VpN changes. Ten units of VpN/2 correspond to 20 kV of ionospheric potential change. For the pressure·area values, 10 units on the plots correspond to about 2 hPa for the 90°-71°N band, and about 0.4hPa for the 51°-31°N band.

4. Hypothesized mechanism

An obvious inference is that the changes in cloud irradiances that correlate with IMF By and overhead ionospheric potential, and that correspond to changes in surface and below-cloud atmospheric temperatures at the same locations, are the cause of the changes in surface pressure that also correlate with B_y in the same locations. However, the phase relationship of the pressure changes to the irradiance changes has yet to be understood. Another direct inference is that the correlations of temperature and pressure in the Antarctic with IMF B_y (Burns et al., 2008; Lam et al., 2013, 2014), and the correlations of irradiance with other sources of ionospheric potential change in the Arctic and Antarctic (Frederick et al., 2019) are caused by the same physical processes, evidently involving electric currents flowing through clouds.

The flow chart in Fig. 21 illustrates the established and hypothesized aspects of the proposed chain of linkages from the solar wind through atmospheric electricity, electro-scavenging and/or electro-anti-scavenging, to tropospheric clouds, radiative coupling and/or latent heat release, to atmospheric dynamics. Discussion of various aspects of these linkages has been made in previous review papers (Tinsley, 1996, 2008; Lam and Tinsley, 2018). Recent papers include those on correlations of surface pressure with By (Zhou et al., 2018) and correlations of irradiance with By (Frederick et al., 2019).

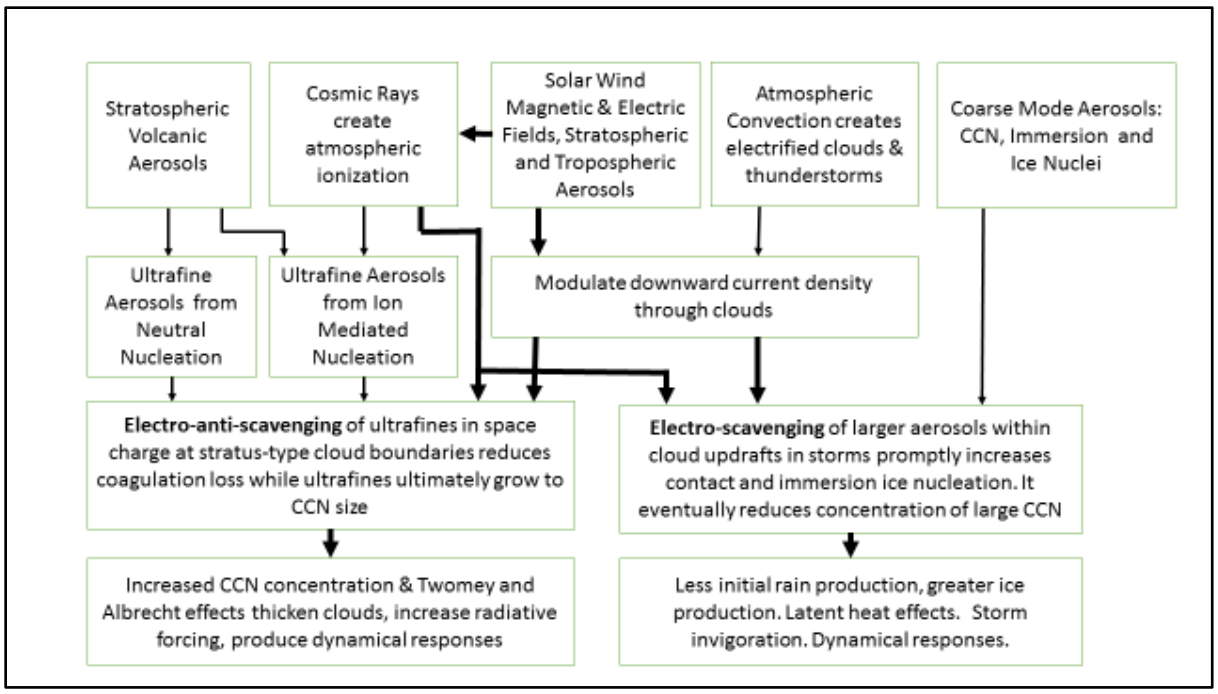

Figure 21. Flow chart of inputs and links influencing atmospheric electric interactions with clouds. Links involving deposition of electric charge on droplets and aerosol particles, influencing the microphysical electro-scavenging and electro-anti-scavenging processes in clouds, are shown in heavier lines.

The cloud microphysical theory underlying the concepts of electroscavenging and electro-anti-scavenging is well known, based on work reviewed, especially in Chapter 18 of the book by Pruppacher and Klett (1997), and more recently extended with numerical modelling in a series of papers by Zhang and Tinsley (2017, 2018), and Zhang et al. (2018, 2019). Electro-scavenging involves the electric image force, and is more applicable to larger droplets and particles. The electro-anti-scavenging process, involving the electric Coulomb force, is the one applicable where space charge is present, and is effective for small and ultrafine aerosol particles and smaller droplets, as in the case of the long-lived stratus-type clouds observed in the high latitudes. As the ionosphere-Earth current density flows through a cloud, here is an accumulation of space charge in the gradients of conductivity at the cloud boundaries (Zhou and Tinsley, 2007, 2012; Mareev, 2008; Nicoll and Harrison, 2016).

Space charge is an excess of charge of one sign, which is required by Poisson's equation to balance the gradient of electric field due to the current flowing through the gradient of conductivity. The conductivity gradient is caused by increasing recombination of air ions on the surfaces of droplets going into the cloud. While Pruppacher and Klett (1997, pp 796-7) showed that to the first order the collision rates aerosol particles with each other was unchanged if there were equal numbers of positive and negative charged particles, this is not the case where there is an excess of charges of one sign. In this case the excess of repulsive encounters reduces the collision rate, and similarly for collisions between particles and small droplets. The lifetime for removal of aerosol particles by Brownian collisions with droplets in a typical cloud is about 40 minutes (Pruppacher and Klett, 1997, p. 723). An excess of charge of one sign can prolong this lifetime, so that over the course of days there is a significant reduction in scavenging. Thus there is an increase in the concentrations of interstitial and evaporation nuclei, and especially in those of the abundant ultrafine aerosol particles (Humphries et al, 2016) in high latitude

upper tropospheric regions, that can mix into the cloud and grow to condensation nuclei size in volatiles contained in the cloud. With increased concentrations of condensation and ice nuclei, during the continual in-cloud microphysical processing during vertical motions associated with cooling at cloud top and warming at cloud base, there is likely to be a significant increase in concentrations and reduction in size of droplets and ice particles. Then the Twomey (1977) effect of increases in cloud opacity could produce increases in optical depth and downward irradiance at high latitudes as observed.

An indication of the strength of the repulsive forces involved in electro-anti-scavenging can obtained by comparing on the one hand the electric potential of charged particle approaching a charged droplet, and on the other hand the thermal kinetic energy of the particle in the line of centers. For q = 1e (1.6×10^{-19}C) on the particle and Q = 50e on a droplet of R = 3 μm radius, and at a temperature of T= 263K we have $Qq/(4\pi\varepsilon_0 R) = 3.75 \times 10^{-21}$ Joules. This can be compared with the average energy of the distribution of the particle velocities in the line of centers; ½kT = 1.8×10^{-21} J, where k is Boltzmann's constant. So collision is inhibited between these same-sign droplets and particles. The comprehensive Monte Carlo simulations, most recently by Zhang et al., (2018, 2019), confirm this.

5. Discussion

The responses of pressure at lower latitudes are approximately opposite to those driven by the solar wind input at higher latitudes, and the geostrophic balance requires changes in zonal wind in between. Observations of the longitudinal distribution of the surface pressure responses by Lam et al., (2013), and in corresponding responses to day-to-day changes in ionospheric potential caused by meteorological generators (Zhou et al., 2018), show that at lower latitudes the zonal mean pressure changes are made up of three or more longitudinal regions of alternating higher and lower amplitude. The larger amplitude of negative pressure excursions are predominantly over oceans in both hemispheres. There is thus the possibility, suggested by Lam et al., (2013), that the low latitude response to the high latitude solar wind forcing includes the modification of Rossby waves by an enhancement in cyclogenesis. Such a feedback process may couple back to higher latitudes to modify the variations phase as well as amplitude of the responses to the quasi-periodic solar wind and cloud longwave irradiance forcing. The dynamical influence of high latitudes on mid-to-low latitudes in each hemisphere is clear from the present work and from previous results. If the influences extend from one hemisphere into the other, then the summer hemisphere responses to the solar wind could affect the phase of the winter hemisphere response. Other possibilities for the phase shifts include the excitation of wave trains of forced pressure oscillations with phase shifts dependent on natural oscillation frequencies.

So far the modeling of electro-anti-scavenging covers only two-body interactions, and the electro-anti-scavenging for size and charge distributions of droplets, ice crystals, and condensation and ice nuclei, and the effects on cloud development, have yet to be modeled. There is a need to model size and electric charge distributions for the mixed particle types, and then to apply parameterized two-body electro-anti-scavenging to the distributions. So the plausibility of the linkages represented by the flow chart has yet to be supported by quantitative modeling, although there is no reason to rule out a result that would give magnitudes and timescales consistent with the observations. The modeling of charge distributions among interacting ions, aerosols, droplets and ice crystals is challenging, especially in the presence of vertical mixing processes in clouds. A beginning for such modelling was made by Yair and Levin (1989).

The changing amplitude and phase of the pressure responses over periods of years seen in Fig. 16 is not understood, and remains a topic for further study. Possibilities include solar cycle changes in other solar wind parameters, for example, the cosmic ray flux; also changes in the concentrations of ultrafine aerosol particles in the upper troposphere in the polar regions, which may be responsive to changes in volcanic activity, and changes in global circulation patterns. It should be noted that the effects analyzed above are for only a fraction of the total ionosphere-earth current density, so the effects of the steady component on cloud microphysics may have been tuned out of models. It will require much further data analysis and modeling to test the above scenarios.

6. Conclusions

Infrared radiances from clouds and from the surface at Alert, Canada, have been analyzed for variations related to solar wind magnetic field time variations, within the solar rotation period and for seasonal and interannual timescales. This work has shown that for periods of 2-sector solar wind structures in the northern hemisphere months (November-March, with less solar insolation) the correlation coefficients, relating both cloud irradiance and surface pressure to ionospheric potential changes driven by the solar wind, markedly increase over the already published statistically significant all-year all-sector-type correlations. The irradiance changes imply changes in optical thickness of the clouds, responding to changes in overhead ionospheric potential that drive vertical current density through clouds.

A longer time series of high and mid-latitude surface pressures, in zonal bands up to 20^{o} of latitude wide, has shown pressure variations of order 1 hPa that are directly attributable to the irradiance changes within the auroral ovals affecting atmospheric temperature and pressure below the clouds, with effects propagating to lower latitudes. The phase relationship of the pressure responses compared to those of the cloud responses are consistent but not understood. A mechanism for the cloud responses to the vertical current density is based on the changing amounts of electrical charges deposited on droplets, ice particles, condensation nuclei and ice nuclei that affect their mutual collision and loss rates. The electro-anti-scavenging process has been extensively modeled for two-body collisions, but there is a need to model size distributions and electric charge distributions for mixed particle types, and then to apply parameterized electro-anti-scavenging processes to the distributions, in order to model changes in cloud development for comparison with the observations.

Acknowledgements and Data Availability Statement: We thank Dr. D. Weimer for helping us to access output from his model, and Drs. W. R. Coley and R.A. Heelis for useful discussions. Dr. Tinsley is a professor emeritus and is self-funded. This work was funded in part by the National Science Foundation of China (41971020, 41905059 and 41571040). The solar wind data is from https://omniweb.gsfc.nasa.gov/form/dx1.html. The reanalysis data is from http://www.noaa.gov/psd/ The Alert irradiance data was obtained from: https://www.esrl.noaa.gov/gmd/dv/data/index.php?category=Radiation&parameter_name=Surface%2BRadiation.

APPENDIX A

Solar wind 2, 4, and irregular/multiple sector structures 1973-2018

2-sector	4-sector	Irregular/multiple sector
1973 Dec 5 – 1975 Oct 17		1975 Oct 18 – 1976 Sept 26
1976 Sept 27 – 1977 July 19		1977 July 20 – 1977 Dec 6
	1977 Dec 7 – 1978 July 4	
1978 July 5 – 1979 Aug 28		1979 Aug 29 – 1980 June 28
	1980 June 29 – 1980 Dec 14	
1980 Dec 15 – 1981 July 19	1981 July 20 – 1982 Jan 12	
1982 Jan 13 – 1982 Dec 6		1982 Dec 7 – 1983 Jan 20
	1983 Jan 21 – 1984 Feb 29	
1984 Mar 1 – 1984 Nov 15	1984 Nov 16 – 1985 Apr 20	
1985 Apr 21 – 1985 Dec 8		1985 Dec 9 – 1987 Apr 30
	1987 May 1 – 1988 Oct 10	
1988 Oct 11 – 1989 May 25	1989 May 26 – 1990 June 1	1990 June 2 – 1993 Oct 26
1993 Oct 27 – 1994 Dec 6	1994 Dec 7 – 1995 June 24	1995 June 25 – 1996 Apr 19
	1996 Apr 20 – 1997 Mar 21	1997 Mar 22 – 1998 Mar 16
	1998 Mar 17 – 1998 Nov 30	
1998 Dec 1 – 1999 May 5	1999 May 6 – 2000 Jan 26	
2000 Jan 27 – 2000 July 13	2000 July 14 – 2001 Mar 25	
2001 Mar 26 – 2001 Sept 21		2001 Sept 22 – 2001 Oct 26
2001 Oct 27 – 2004 July 19	2004 July 20 – 2007 Aug 14	
2007 Aug 15 – 2008 Dec 17		2008 Dec 18 – 2010 Jan 10
2010 Jan 11 – 2010 Apr 12	2010 Apr 13 – 2011 Feb 28	
2011 Mar 1 – 2011 Dec 17	2011 Dec 18 – 2012 Sept 7	2012 Sept 8 – 2013 Feb 12
2013 Feb 13 – 2013 June 23	2013 June 24 – 2014 Oct 17	
2014 Oct 18 – 2015 Feb 22		2015 Feb 23 – 2015 June 7
2015 June 8 – 2016 Jan 17	2016 Jan 18 – 2016 Apr 1	
2016 Apr 2 – 2017 Mar 31		2017 Apr 1 – 2017 Oct 27
2017 Oct 28 – 2018 June 29		2018 June 30 – 2018 Nov 3

APPENDIX B. The effects of IMF B_z and solar wind speed (Vsw), as well as IMF B_y, on polar cap potentials

Introduction

Figure B1 shows plots of northern hemisphere solar wind-induced polar cap ionospheric potentials from the satellite-based empirical models Weimer (1996), as functions of magnetic latitude and magnetic local time, for four sets of values of IMF B_y and B_z. They all have the same total solar wind magnetic field, $B_T = \sqrt{(B_y^2 + B_z^2)} = 5$nT, and the same solar wind speed, Vsw = 450 kms^{-1}). These solar wind - induced potential for these cases range from +20 kV to -49 kV and are measured as offsets from the global ionospheric potential (relative to the Earth's surface) of about 250 kV generated by thunderstorms and highly electrified shower clouds. The global component has its own diurnal and seasonal and day-to-day variations due to variations in convective storm output. In Fig B1(a) and B1(c) , which are for positive By (+4.5 nT), the solar wind imposed potential close to the north magnetic pole (marked with a black dot) is negative. The potential at the pole changes to positive in B1(b) and B1(d) with negative B_y (-4.5 nT).

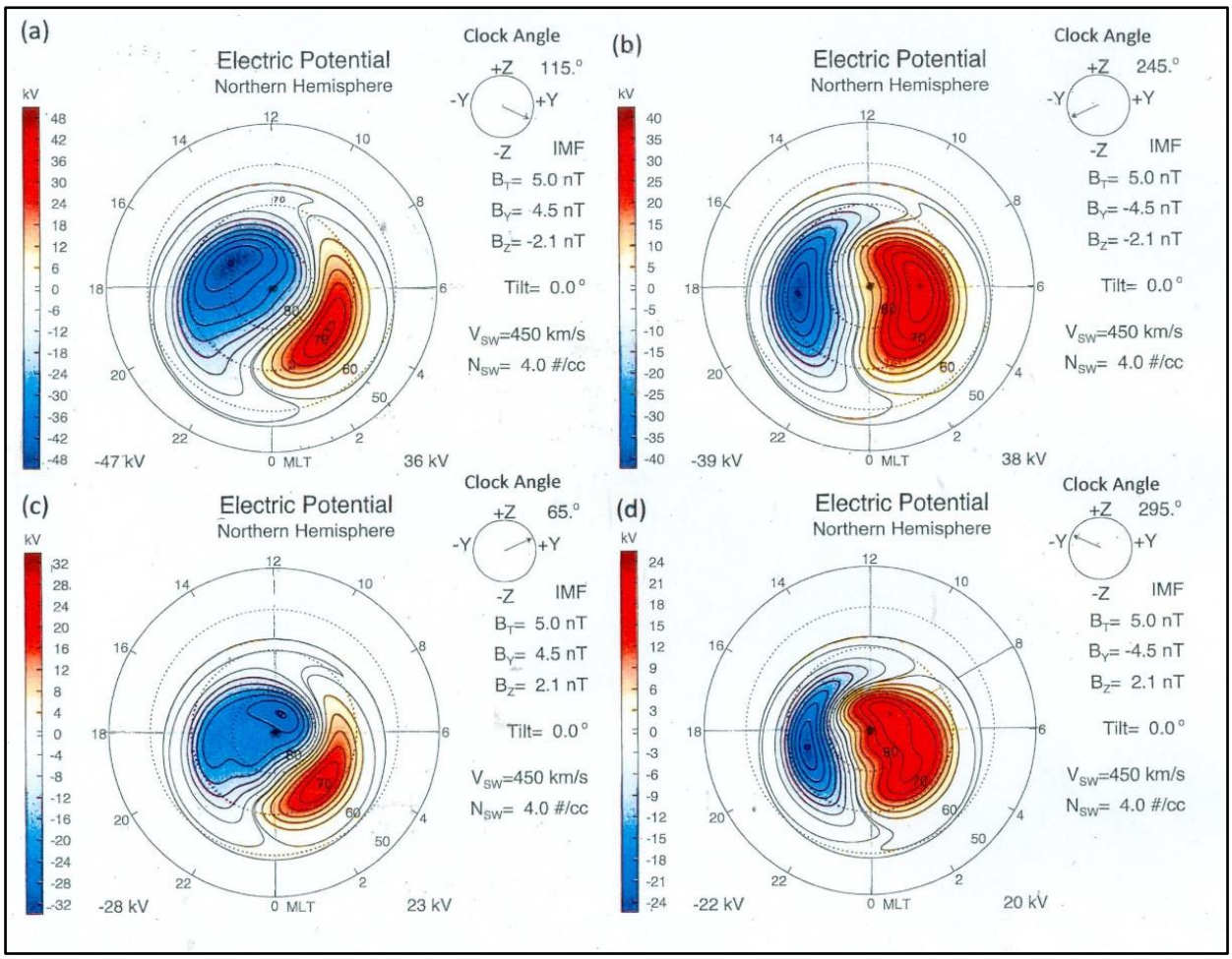

Figure B1. Solar wind–induced potential distributions over the northern polar cap as functions of magnetic latitude and magnetic local time. The data is from the empirical model of satellite observations by Weimer (1996). In each case the total transverse IMF is 5 nT; the solar wind speed Vsw is 450 kms^{-1}; the plasma number density is 4 ions/cc., and the tilt of the polar axis with respect to the equatorial plane is zero. The four seta are for four different combinations of IMF B_y and IMF B_z, with (a) and (c) for positive B_y and (b) and (d) for negative B_y. With (a) and (b) the B_z component is negative, while for (c) and (d) it is positive, as indicated on the clock angle insert.

It is well known that the magnitudes of the dawn and dusk side convection cells depend on the B_z component and also on Vsw. The sign of B_z is negative in B1(a) and B1(b) and positive in B1(c) and B1(d). The magnitude of the overall potentials for both the dawn and dusk convection cells are greater in B1(a) and B1(b) with negative (southward) B_z than for positive B_z (northward). So we should expect to see an improvement in correlation coefficients if we correlate meteorological variables not with B_y only, but with a representation of the potential that takes into account the effects of Vsw and B_z. These effects are lost, for example, when we take correlations with B_y, or pressure averages for B_y < -3 nT from pressure averages for B_y > 3nT over months or years (Burns et al., 2008; Lam et al., 2013).

So in this exercise we will parameterize the potentials at the magnetic pole with B_z and Vsw as well as with B_y. Also, in analyses of zonal mean surface pressures (Lam et al., 2013; Zhou and Tinsley, 2018), we need to take into account that the solar wind effect is averaged over large areas of the polar atmospheres. A representation is needed for the integral of the potentials over the whole polar caps, to

see if that would improve correlation coefficients for the broad effect of the polar cap potentials over such large areas. Thus we will also parameterize these area-integrated potentials.

Parameterization for North Pole Potential.

Table B1 gives the solar wind-induced potential at the north magnetic pole as a function of B_T, Vsw, and clock angle θ. This angle is defined by the signs and magnitudes of B_y and B_z in four quadrants, increasing clockwise (contrary to the analytical geometry convention of angle increasing anti-clockwise). For B_y +ve and B_z +ve, $\theta = \tan^{-1}|B_y/B_z|$. For B_y +ve and B_z -ve, $\theta = 180^o - \tan^{-1}|B_y/B_z|$. For By –ve and B_z –ve, $\theta = 180^o + \tan^{-1}|B_y/B_z|$. For B_y –ve and B_z +ve, $\theta = 360^o - \tan^{-1}|B_y/B_z|$. The use of clock angle for ordering the potentials was found by Weimer to give a better empirical model than ordering by B_z and B_y separately. All the sets are for a fixed solar wind plasma density of 4 cm^{-3}.

Table B1

Clock angle θ	300 kms^{-1}, B_T = 5nT	300 kms^{-1}, B_T =10nT	450 kms^{-1}, B_T = 5nT	450 kms^{-1}, B_T = 10nT	800 kms^{-1}, B_T = 5nT.	800 kms^{-1}, B_T = 10nT
25^o	-8.5	-9.6	-9.0	-8.0	-8.0	-6
45^o	-15.5	-17.5	-15.7	-17.4	-15.6	-17.3
65^o	-21.5	-25.5	-21.7	-26.4	-23.5	-28.7
90^o	-25.0	-32.5	-27.4	-34.5	-30.5	-38.5
115^o	-27.0	-35.0	-29.1	-37.1	-32.5	-41.5
135^o	-25.0	-32.0	-27.3	-34.4	-30.0	-37.9
155^o	-22.0	-26.0	-24.0	-29.0	-25.0	-29.0
180^o	-15.0	-16.0	-15.0	-15.0	-13.0	-14.0
205^o	-6.5	-4.0	-4.0	-1.0	0.0	4.0
225^o	0.0	6.5	3.2	10.4	9.0	17.5
245^o	4.0	14.0	9.0	19.1	16.5	28.4
270^o	7.7	17.0	12.9	24.9	21.9	35.9
295^o	7.0	18.0	12.7	24.9	21.9	36.4
315^o	5.0	15.2	10.0	21.0	18.6	31.9
335^o	1.8	9.0	6.3	11.0	13.5	24.0
360^o	4.0	0.5	-1.5	6.0	3.0	10.0

From Table B1 we see that for $45° \le \theta \le 335°$, for fixed clock angles, the magnitude of the potentials increase as B_T goes from 5 nT to 10 nT, as expected, but they also increase with Vsw. The absolute magnitudes of the values are larger at clock angle 90^o (B_y = 5nT, B_z = 0) than at 270^o (B_y = –5nT, B_z = 0).

Values from Table B1 are plotted in Fig. B2, and we see that these north magnetic pole potentials are more negative for B_y +ve than they are positive for B_y -ve. Also, the relative variation with B_T and Vsw is much greater for the smaller positive potentials with B_y -ve than for the larger negative potentials with B_y +ve. Also, for B_y +ve the magnitude of the potentials increase with B_z -ve and with Vsw. For B_y -ve they increase with B_z +ve and with Vsw.

This analysis also applies to the southern polar cap, but with the sign of B_y reversed.

The variations in polar potential with Vsw and B_z are sufficiently large that we expect that taking them into account would improve the correlations that have so far been found for surface pressure and cloud opacity with B_y only, for stations near the north and south magnetic poles

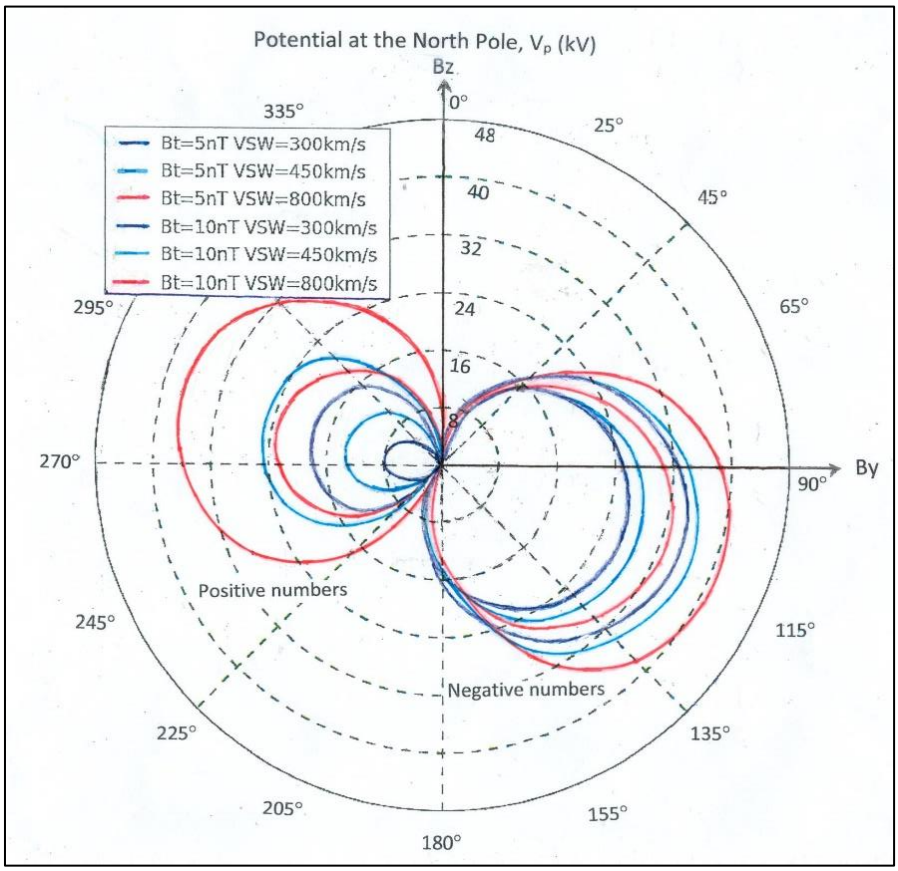

Figure B2. The solar wind – induced potential at the north magnetic pole, for the six sets of B_T, V_{SW} and clock angles listed in Table B1. The value of B_y (horizontal axis) and B_z (vertical axis) for a given B_T determine the clock angle θ. If both are positive, $\theta = \tan^{-1}(B_y/B_z)$.

Empirical fits to the curves of Fig. B2 are based on a perturbation analyses referred to two potential values that are typical in the solar wind when B_y is either positive or negative, corresponding to the potential being either negative or positive at the north magnetic pole. Vsw is never much below 300 m/s, and cases where B_y is near zero are relatively few, as the solar wind is characterized by the Parker spiral structure, with magnetic sectors either towards the sun or away, corresponding to opposite signs of B_y. The bimodal nature of B_y is illustrated in Frederick et al. (2019, Fig. 3). We define the empirical fits in terms of expressions consisting of the product of an amplitude function, V_{pa}, and a phase function P_p, i.e. $V_p = V_{pa}P_p$.

For the situations where the net polar potential is positive, we define the amplitude function, V_p^+, in terms of perturbations from a reference potential, V_{p0}^+, which is the maximum value for B_T = 5 nT, Vsw = 450 kms^{-1}, and is at clock angle θ = 283°, so that V_{p0}^+ = 13.26 kV. Varying positive polar potentials V_p^+ are then fitted in terms of $\Delta B_T = (B_T - 5nT)$; $\Delta Vsw = (Vsw - 450\ kms^{-1})$ and θ, for the range of θ determined by the signs of the values in Table 1, with the amplitude function V_{pa}^+ given by:

$V_{pa}^{+} = 13.26 + 2.38(\Delta B_T) + \{0.033096 + 2.6162x10^{-3}(\Delta B_T)\}\Delta Vsw - \{2.1581x10^{-5} + 3.9810x10^{-6}(\Delta B_T)\}(\Delta Vsw)^2$ kV …… …… …… (1)

and a phase function given by:

$P_p^{+} = \sin^2(\theta - 13^o - 3^o\cos(\theta - 13^o))$ ….. ….. …… (2)

For net negative polar potentials, the reference potential is V_{p0}^{-}, which is the maximum (negative) value with B_T = 5 nT, Vsw = 450 kms^{-1}, at clock angle $\theta = 112^o$, so that $V_{p0}^{-} = -29.15$ kV. Varying negative polar potentials V_p^{-} are then fitted in terms of ΔB_T, ΔVsw and θ, for the range of θ determined by the signs of the values in Table 1, with the amplitude function V_{pa}^{-} given by:

$V_{pa}^{-} = -29.15 - 1.59(\Delta B_T) - \{0.012896 + 1.3756x10^{-4}(\Delta B_T)\}\Delta Vsw - \{9.58095x10^{-6} + 1.2724x10^{-6}(\Delta B_T)\}(\Delta Vsw)^2$ …. …. …. (3)

and a phase function given by :

$P_p^{-} = \sin^2(\theta - 22^o - 25^o\cos(\theta - 22^o))$ kV ….. ….. (4)

Inspecting Table B1 for the sign of the potentials as a function of the clock angle θ, we see that for a few clock angles near the transitions in sign and with smaller potential values the signs change with Vsw and B_T. A range of clock angles which avoids all but a few minor cases of these, and can be used to define the main range for V_p^{-}, is for clock angles 15° to 200°. Similarly, a range of clock angles that can be used to define V_p^{+} is for clock angles 220° to 355°. These are non-overlapping, and the values of V_p^{-} and V_p^{+} can be merged to create a single series for potential V_p at a pole as a function of clock angle.

Parameterization for Area-Integrated Potential.

The parameterization for the area-integrated potential over the whole polar cap is based on numerical data for the above six sets of B_T and Vsw from Weimer (1996), for each of 16 clock angles. The area integrals are in units of 10^8 kV km^2, and were made separately for areas of negative (largely on the dusk side) and positive (largely on the dawn side) potential, and are shown in Table B2, with their algebraic sum given in the fourth column of each panel. The values of B_T used were 5 nT and 10 nT, and those of The solar wind plasma density Nsw was constant at 4 cm^{-3}.The numerical results are given in Table 2, and together with additional results for B_T = 7.5 nT, are plotted in Fig. B3.

Vsw used were 300 kms^{-1}, 450 kms^{-1} and 800 kms^{-1}.

BT=5 VSW=300 NSW=4				BT=10 VSW=300 NSW=4				BT=7.5 VSW=300 NSW=4			
θ	negative		total	θ	negative	positive	total	θ	negative	positive	total
0	-3.7277e+07	2.5153e+07	-1.2125e+07	0	-2.5332e+07	2.5336e+07	4.5855e+03	0	-2.9058E+07	2.4077E+07	-4.9811E+06
25	-5.5867e+07	2.9811e+07	-2.5855e+07	25	-4.8348e+07	2.7902e+07	-2.0446e+07	25	-5.1602E+07	2.8594E+07	-2.3008E+07
45	-7.9452e+07	3.6806e+07	-4.2646e+07	45	-8.5527e+07	3.8434e+07	-4.7094e+07	45	-8.2820E+07	3.7587E+07	-4.5232E+07
65	-1.1202e+08	4.6835e+07	-6.5186e+07	65	-1.3991e+08	5.4825e+07	-8.5086e+07	65	-1.2699E+08	5.1039E+07	-7.5952E+07
90	-1.6257e+08	6.4416e+07	-9.8155e+07	90	-2.2770e+08	8.4856e+07	-1.4284e+08	90	-1.9870E+08	7.5739E+07	-1.2296E+08
115	-2.1172e+08	8.6985e+07	-1.2474e+08	115	-3.2227e+08	1.2701e+08	-1.9526e+08	115	-2.7356E+08	1.0953E+08	-1.6402E+08
135	-2.4001e+08	1.0750e+08	-1.3251e+08	135	-3.8215e+08	1.6802e+08	-2.1414e+08	135	-3.1708E+08	1.4030E+08	-1.7678E+08
155	-2.5213e+08	1.2817e+08	-1.2396e+08	155	-4.0818e+08	2.0947e+08	-1.9871e+08	155	-3.3676E+08	1.7172E+08	-1.6504E+08
180	-2.4040e+08	1.4840e+08	-9.1994e+07	180	-3.8622e+08	2.4875e+08	-1.3746e+08	180	-3.1866E+08	2.0216E+08	-1.1650E+08
205	-2.0234e+08	1.5269e+08	-4.9652e+07	205	-3.1832e+08	2.6063e+08	-5.7693e+07	205	-2.6426E+08	2.1098E+08	-5.3286E+07
225	-1.6447e+08	1.4341e+08	-2.1059e+07	225	-2.4853e+08	2.4492e+08	-3.6171e+06	225	-2.0986E+08	1.9815E+08	-1.1706E+07
245	-1.2751e+08	1.2498e+08	-2.5368e+06	245	-1.7986e+08	2.0816e+08	2.8306e+07	245	-1.5695E+08	1.7105E+08	1.4107E+07
270	-8.7718e+07	9.4241e+07	6.5228e+06	270	-1.1027e+08	1.4942e+08	3.9146e+07	270	-9.9885E+07	1.2453E+08	2.4648E+07
295	-5.8474e+07	6.3459e+07	4.9847e+06	295	-6.2774e+07	9.5389e+07	3.2615e+07	295	-6.0139E+07	8.0843E+07	2.0705E+07
315	-4.3402e+07	4.4359e+07	9.5603e+05	315	-3.9091e+07	6.2418e+07	2.3327e+07	315	-4.0467E+07	5.4389E+07	1.3922E+07
335	-3.4798e+07	3.0898e+07	-3.8994e+06	335	-2.6117e+07	3.9685e+07	1.3569e+07	335	-2.9413E+07	3.5970E+07	6.5570E+06

BT=5 VSW=450 NSW=4				BT=10 VSW=450 NSW=4				BT=7.5 VSW=450 NSW=4			
θ	negative	positive	total	θ	negative	positive	total	θ	negative	positive	total
0	-4.3842e+07	3.5051e+07	-8.7906e+06	0	-3.3145e+07	4.1135e+07	7.9893e+06	0	-3.6673e+07	3.7645e+07	9.7239e+05
25	-7.3944e+07	4.0648e+07	-3.3296e+07	25	-6.5269e+07	3.9387e+07	-2.5882e+07	25	-6.9397e+07	3.9898e+07	-2.9499e+07
45	-1.1346E+08	5.1175E+07	-6.2286E+07	45	-1.2304E+08	5.4441E+07	-6.8596E+07	45	-1.1885e+08	5.2932e+07	-6.5917e+07
65	-1.6661E+08	6.6401E+07	-1.0021E+08	65	-2.0557E+08	7.7882E+07	-1.2769E+08	65	-1.8727e+08	7.2398e+07	-1.1487e+08
90	-2.4723E+08	9.3289E+07	-1.5394E+08	90	-3.3556E+08	1.2095E+08	-2.1462E+08	90	-2.9605e+08	1.0852e+08	-1.8754e+08
115	-3.2379E+08	1.2834E+08	-1.9545E+08	115	-4.7139E+08	1.8132E+08	-2.9007E+08	115	-4.0642e+08	1.5826e+08	-2.4816e+08
135	-3.6633E+08	1.6090E+08	-2.0543E+08	135	-5.5520E+08	2.4107E+08	-3.1413E+08	135	-4.6871e+08	2.0431e+08	-2.6440e+08
155	-3.8281e+08	1.9453e+08	-1.8827e+08	155	-5.8919e+08	3.0240e+08	-2.8679e+08	155	-4.9488e+08	2.5229e+08	-2.4259e+08
180	-3.6200e+08	2.2932e+08	-1.3267e+08	180	-5.5416e+08	3.6288e+08	-1.9128e+08	180	-4.6538e+08	3.0107e+08	-1.6431e+08
205	-3.0209e+08	2.4057e+08	-6.1512e+07	205	-4.5596e+08	3.8592e+08	-7.0043e+07	205	-3.8425e+08	3.1926e+08	-6.4988e+07
225	-2.4412E+08	2.3005E+08	-1.4068E+07	225	-3.5638E+08	3.6806E+08	1.1680E+07	225	-3.0480e+08	3.0455e+08	-2.4610e+05
245	-1.8747E+08	2.0361E+08	1.6131E+07	245	-2.5812E+08	3.1791E+08	5.9784E+07	245	-2.2756e+08	2.6719e+08	3.9622e+07
270	-1.2637E+08	1.5608E+08	2.9702E+07	270	-1.5781E+08	2.3324E+08	7.5428E+07	270	-1.4351e+08	1.9851e+08	5.4994e+07
295	-8.1184E+07	1.0633E+08	2.5150E+07	295	-8.8502E+07	1.5239E+08	6.3884E+07	295	-8.4433e+07	1.3143e+08	4.6996e+07
315	-5.7595E+07	7.4267E+07	1.6672E+07	315	-5.3515E+07	1.0146E+08	4.7944E+07	315	-5.4914e+07	8.9553e+07	3.4639e+07
335	-4.3841e+07	5.0693e+07	6.8520e+06	335	-3.4021e+07	6.5178e+07	3.1157e+07	335	-3.7819e+07	5.9144e+07	2.1326e+07

BT=5 VSW=800 NSW=4				BT=10 VSW=800 NSW=4				BT=7.5 VSW=800 NSW=4			
θ	negative	positive	total	θ	negative	positive	total	θ	negative	positive	total
0	-8.6640e+07	8.3062e+07	-3.5778e+06	0	-7.1051e+07	1.0245e+08	3.1397e+07	0	-7.6623E+07	9.2595E+07	1.5972E+07
25	-1.4614e+08	8.2660e+07	-6.3478e+07	25	-1.3227e+08	8.3710e+07	-4.8562e+07	25	-1.3871E+08	8.2396E+07	-5.6309E+07
45	-2.3272e+08	1.0136e+08	-1.3136e+08	45	-2.5406E+08	1.0939E+08	-1.4467E+08	45	-2.4428E+08	1.0557E+08	-1.3871E+08
65	-3.4566e+08	1.2904e+08	-2.1662e+08	65	-4.2326E+08	1.5208E+08	-2.7118E+08	65	-3.8555E+08	1.4086E+08	-2.4469E+08
90	-5.1089e+08	1.7946e+08	-3.3143e+08	90	-6.7719E+08	2.3073E+08	-4.4646E+08	90	-6.0049E+08	2.0699E+08	-3.9350E+08
115	-6.6103e+08	2.4773e+08	-4.1330e+08	115	-9.2896E+08	3.4242E+08	-5.8654E+08	115	-8.0797E+08	3.0024E+08	-5.0773E+08
135	-7.4010e+08	3.1423e+08	-4.2587e+08	135	-1.0756E+09	4.5557E+08	-6.2006E+08	135	-9.1870E+08	3.8945E+08	-5.2926E+08
155	-7.6651e+08	3.8663e+08	-3.7989e+08	155	-1.1280e+09	5.7613e+08	-5.5183e+08	155	-9.5972E+08	4.8620E+08	-4.7352E+08
180	-7.1914e+08	4.6706e+08	-2.5207e+08	180	-1.0534e+09	7.0274e+08	-3.5068e+08	180	-8.9602E+08	5.9157E+08	-3.0446E+08
205	-6.0019e+08	5.0489e+08	-9.5297e+07	205	-8.6995e+08	7.6619e+08	-1.0376e+08	205	-7.4199E+08	6.4445E+08	-9.7546E+07
225	-4.8745e+08	4.9555e+08	8.0927e+06	225	-6.8713E+08	7.4881E+08	6.1686E+07	225	-5.9371E+08	6.2994E+08	3.6230E+07
245	-3.7730e+08	4.5041e+08	7.3106e+07	245	-5.0502E+08	6.6463E+08	1.5962E+08	245	-4.4853E+08	5.6706E+08	1.1853E+08
270	-2.5656e+08	3.5678e+08	1.0022e+08	270	-3.1599E+08	5.0728E+08	1.9129E+08	270	-2.8847E+08	4.3767E+08	1.4920E+08
295	-1.6620e+08	2.5235e+08	8.6146e+07	295	-1.8193E+08	3.4682E+08	1.6489E+08	295	-1.7329E+08	3.0228E+08	1.2899E+08
315	-1.1808e+08	1.8130e+08	6.3218e+07	315	-1.1181E+08	2.3968E+08	1.2787E+08	315	-1.1420E+08	2.1313E+08	9.8928E+07
335	-8.8925e+07	1.2584e+08	3.6913e+07	335	-7.2382e+07	1.6000e+08	8.7620e+07	335	-7.9164E+07	1.4511E+08	6.5944E+07

Table B2. Northern polar cap area-integrated potentials as a function of transverse the clock angle θ, for nine sets of values of solar wind magnetic field B_T in nT and solar wind speed V_{SW} in km/s. The units of the area-integrated potential are 10^8 kV·km^2.

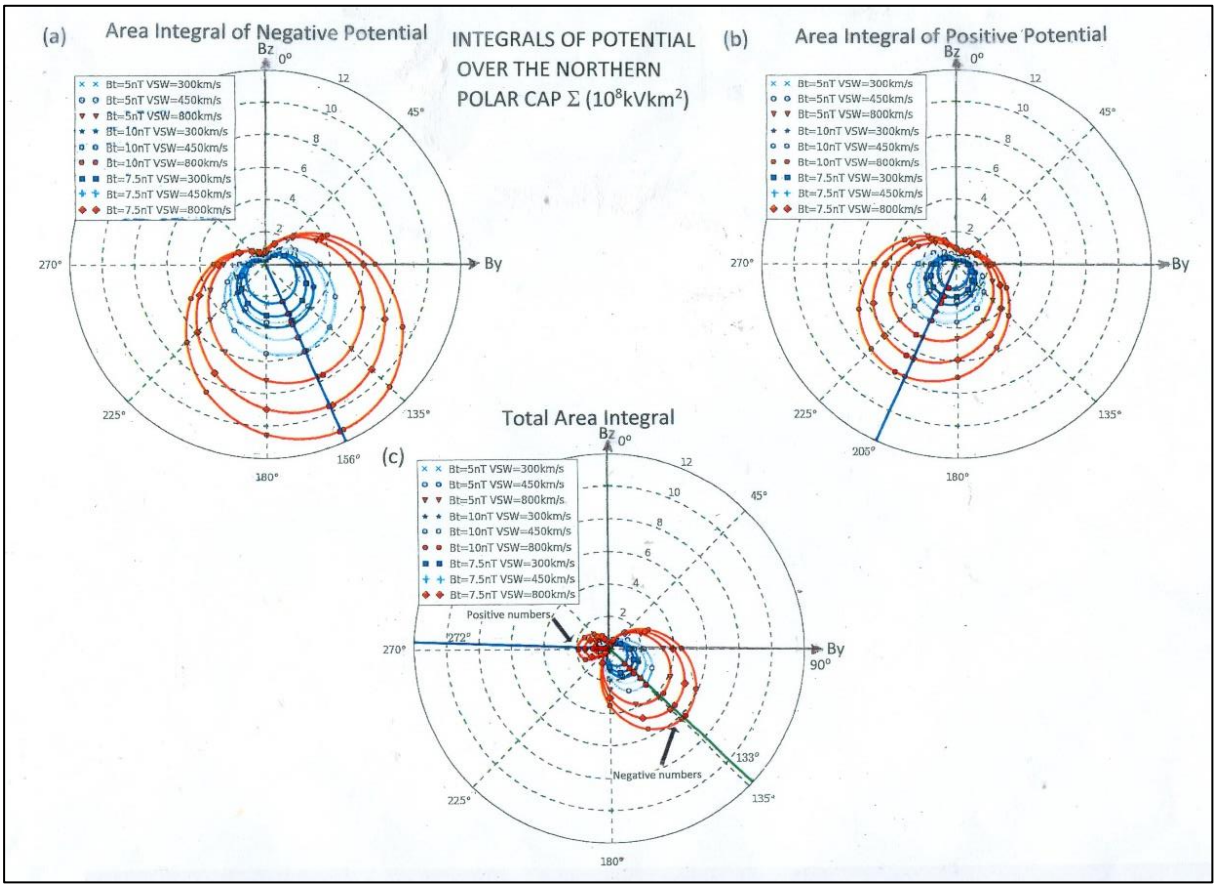

Figure B3. Integrals of potential over the area of the northern polar cap Σ are given as a function of the clock angle θ for B_T values 5nT, 7.5nT, and 10 nT, with V_{SW} values of 300, 450, and 800 km/s. In (a) the integral is only over negative potentials, while in (b) it is only over positive potentials, and in (c) the integral is over the whole polar cap, i.e., the algebraic sum of (a) and (b). The units of the area-integrated potential are 10^8 kV·km^2.

The integrals of negative potential, Fig. B3(a), are generally larger in absolute magnitude than those for positive potential, Fig. B3(b), and both are considerably larger than the algebraic sum, Fig. B3(c). From Fig. B3(c) we see that the total integral varies strongly with Vsw and B_T. The smaller lobe from θ = 225° to 25° is for a positive total, and is largely for B_y negative, with B_z both positive and negative. The larger lobe, from θ = 25° to 225°, is for a negative total, and is largely for B_y positive with B_z negative. Almost complete cancellation occurs for Vsw = 300 kms^{-1} with B_T = 5 nT, so that the values are nearly zero close to the origin, with maximum value (from Table B2) of 0.065x10^8 kV km^2.

Discussion

The above expressions are derived for the northern polar cap. For use in the southern polar cap the sign of B_y should be reversed in the expressions. The expressions for the potential V_p at the magnetic poles should be applicable to analyses of observations made close to the poles, such as at Alert in northern Canada, and Vostok in Antarctica (Burns et al., 2007, 2008; Frederick et al., 2019). The expressions for the area integrated potentials should be applicable to analyses of zonal mean pressure variations, e.g., those of Lam et al., (2013) and Zhou et al., (2018). While the solar wind input is a

function of magnetic latitude, the atmospheric circulation is a function of geographic latitude, and tends to smear out the local inputs.

Correlations of meteorological parameters with Vsw and B_z have been observed by Boberg and Lundstedt (2003) on the seasonal and decadal timescale. It is possible that these correlations would be improved by using parameters such as $\Sigma^+ \text{ and } \Sigma^-$ instead of functions of Vsw and B_z only. Also, for superposed epoch analyses of meteorological data around solar wind sector boundaries, the effects of the ionospheric potential changes will be affected by the systematic reductions in Vsw and reductions in magnetic activity (related to less negative B_z) that have been observed at times of sector boundary passage.

References

Boberg, F., and H. Lundstedt, 2003. Solar wind electric field modulation of the NAO: A correlation analysis in the lower atmosphere. Geophys. Res. Lett., 30 (15) 1825, doi10.1029/2003GL017360

Burns, G. B., B. A. Tinsley, A. R. Klekociuk, O. A. Troshichev, A. V. Frank-Kamenetsky, M. J. Duldig, E. A. Bering, J. M. Clem, 2006. Antarctic polar plateau vertical electric field variations across heliocentric current sheet crossings, J. Atmos. Solar-Terr. Phys., 68, 639-654. Doi:10.1016/j.jastp.2005.10.008.

Burns, G. B., Tinsley, B. A., French, W. J. R., Frank-Kamenetsky, A. V., Bering, E. A. 2007. Interplanetary magnetic field and atmospheric electric circuit influences on ground-level pressure at Vostok. J. Geophys. Res. 112, D04103, https:// doi.org/10.1029/2006JD007246.

Burns, G. B., Tinsley, B. A., French, W. J. R., Troshichev, O. A., Frank-Kamenetsky, A. V., 2008. Atmospheric circuit influences on ground-level pressure in the Antarctic and Arctic. J. Geophys. Res. 113, D15112, https:// doi.org/10.1029/2007JD009618.

Frederick, J.E., Tinsley, B.A., 2018. The response of longwave radiation at the South Pole to electrical and magnetic variations: Links to meteorological generators and the solar wind. J. Atmos. Sol. Terr. Phys. 179, 214-224. https://doi.org/10.1016/j/jastp.2018.08.003.

Frederick, J.E., Tinsley, B.A., and Zhou, L., 2019. Relationships between the solar wind magnetic field and ground-level longwave irradiance at high northern latitudes. J. Atmos. Sol. Terr. Phys. 193,105063. doi:.org/10.1016/j.jastp.2019.105063.

Hays. P. B., and Roble, R.G., 1979, A quasi-static model of global atmospheric electricity; 1. The lower atmosphere. J. Geophys. Res., 84, 3291 -3305.

Humphries, R.S., Klekociuk, A.R., Schofield, R., Keywood, M., Ward, J., Wilson, S.R., 2016. Unexpectedly high ultrafine aerosol concentrations above East Antarctic sea ice. Atmos. Chem. Phys. 16, 2185–2206. http://dx.doi.org/10.5194/acp-16-2185-2016.

Kalnay, E., Kanamitsu, M., Kistler, R., et al., 1996. The NCEP/NCAR 40-year reanalysis project. Bull. Am. Meteorol Soc., 77, 437-471

Lam, M. M., and B. A. Tinsley, 2016. Solar wind – atmospheric electricity – cloud microphysics connections to weather and climate, J. Atmos. Solar-Terr. Phys., 149, 277-290. doi.org/10.1016/j.jastp.2015.10.01.

Lam, M.M., Chisham, G., Freeman, M.P., 2013. The interplanetary magnetic field influences mid-latitude surface atmospheric pressure. Environ. Res. Lett. 8, 045001. https://doi.org/10.1088/1748-9326/8/4/045001.

Lam, M.M., Chisham, G., Freeman, M.P., 2014. Solar wind-driven geopotential height anomalies originate in the Antarctic lower troposphere. Geophys. Res. Lett. 41, 6509-6514. doi:10.1002/2014GL061421.

Mansurov, S. M., Mansurova, L. G., Mansurov, G. S., Mikhenvich, V. V., Visotsky, A. M. 1974. North-south asymmetry of geomagnetic and tropospheric events, J. Atmos. Solar-Terr. Phys., 36, 957-962.

Mareev, E.A., 2008. Formation of charge layers in the planetary atmospheres, Space Sci. Rev, 137. 373-393.

Markson, R. 1983. Solar modulation of fair-weather and thunderstorm electrification and a proposed program to test an atmospheric electrical sun-weather relationship, p.323-343 in “Weather and Climate Responses to Solar Variations”, Colorado Associated University Press, Boulder Co. 626 pp.

Mauritsen, T., Sedlar, J., Tjernström, M., Leck, C., Martin, M., Shupe, M., Sjogren, S., Sierau, B., Persson, P. O. G., Brooks, I. M., Swietlicki, E., 2011. An Arctic CCN-limited cloud-aerosol regime. Atmos. Chem. Phys. 11, 165-173. https://doi.org/10.5194/acp-11-165-2011.

NASA/Goddard Space Flight Center, 2018. Space Physics Data Facility OMNIWeb Internet database, available at https://omniweb.gsfc.nasa.gov/form/dx1.html

Ness, N.F., and Wilcox, J. M., 1965. Sector structure in the quiet interplanetary magnetic field, Science, 148, 1592-1594.

Nicoll, K. A., Harrison, R. G., 2016. Stratiform cloud electrification: Comparison of theory with multiple in-cloud measurements, Quart. J. Roy. Meteorol. Soc., 142 (700), 2679-2691. doi.org/10.1002/qj2858.

NOAA, Earth System Research Laboratory, 2018. Surface radiation database, available at https://www.esrl.noaa.gov/gmd/dv/data/index.php?category=Radiation&parameter_name=Surface%2BRadiation

NOAA/NCEP reanalysis data, http://www.noaa.gov/psd/

Pruppacher, H. R., Klett, J.D., 1997. Microphysics of Clouds and Precipitation. 2nd Ed., Springer, London.

Ramanathan, V., Subilsar, B., Zhang, G. J., Conat, W., Cess., R. D., Kiehl, J. T., Grassi, H., Shi, L., 1995. Warm pool heat budget and shortwave cloud forcing: A missing physics? Science, 267, 499-503.

Roble, R. G., and Hays, P. B., 1979. A quasi-static model of global atmospheric electricity; 2. Electrical coupling between the upper and lower atmosphere, J. Geophys. Res. 84, 7247-7256.

Tinsley, B.A., 2008. The global atmospheric electric circuit and its effects on cloud microphysics. Rep. Prog. Phys. 71, 066801. https://doi.org/10.1088/0034-4885/71/6/066801.

Tinsley, B.A., Heelis, R.A., 1993. Correlations of atmospheric dynamics with solar activity: evidence for a connection via the solar wind, atmospheric electricity, and cloud microphysics. J. Geophys. Res. 98, 10375-10384.

Twomey, B., 1977.The influence of pollution on the shortwave albedo of clouds, J. Atmos. Sci., 34, 1149-1152.

Yair, Y., and Levin, Z, 1989. Charging of polydispersed aerosol particles by attachment of atmospheric ions. J. Geophys. Res., 94, D11, 13,085-13,091.

Wilcox, 1. M., Scherrer, P. H., Svalgaard, L., Roberts, W.O., and Olson, R. H., 1973. Solar magnetic structure: relation to circulation of the Earth's atmosphere, Science, 180, 185-186, 1973.

Zhang, L., and Tinsley, B. A., 2017. Parameterization of aerosol scavenging due to atmospheric ionization under varying relative humidity, J. Geophys. Res. Atmos., 122, 5330-5350. doi:10.1002/2016/JD026255.

Zhang, L., and Tinsley, B. A., 2018. Parameterization of aerosol scavenging due to atmospheric ionization: 2 Effects of varying particle density, J. Geophys. Res. Atmos., 123, 3099-3115. doi:10.1002/2017/JD027884.

Zhang, L., Tinsley, B.A., Zhou, L., 2018. Parameterization of in-cloud aerosol scavenging due to atmospheric ionization, Part 3. Effects of varying droplet radius. J. Geophys. Res. Atmos. 123, 10,546-10,567. https://doi.org/10.1029/2018JD028840.

Zhang, L., Tinsley, B.A., Zhou, L., 2019. Parameterization of in-cloud aerosol scavenging due to atmospheric ionization, Part 4. Effects of varying altitude. J. Geophys. Res. Atmos. 124, 13,105-13126. https://doi.org/10.1029/2018JD030126.

Zhou, L., Tinsley, B.A., 2007. Production of space charge at the boundaries of layer clouds. J. Geophys. Atmos. 112, D11203, doi:10.1029/2006JD007998. https://doi.org/10.1029/2006JD007998.

Zhou, L, and Tinsley, B. A., 2012. Time dependent charging of layer clouds in the global electric circuit. Adv. Space Res., 50, 828-842. Doi:10.1016/j.asr.2011.12018.

Zhou, L., Tinsley, B.A., Wang, L., Burns, G., 2018. The zonal-mean and regional tropospheric pressure responses to changes in ionospheric potential. J. Atmos. Solar-Terr. Phys., 171, 111-118, http://dx.doi.org/10.1016/j.jastp.2017.07.010.

Weimer, D. R., 1996. A flexible, IMF dependent model of high latitude electric potentials having "space weather" applications. Geophys. Res. Lett., 23(18), 2549-2552.

Captions for figures

Figure 1. Time series of IMF By (top panel), IMF Bz (middle panel) and solar wind speed (lower panel) July 2005 to June 2009, from NASA (2018). Intervals of sector structure are designated 2-sector, 4-sector or variable (irregular or more than 4 sectors).

Figure 2. Diagrams of East-West sections through the northern hemisphere of the global electric circuit, from (top) Markson (1983) showing the dawn and dusk ionospheric potential changes induced by IMF Bz, and (bottom) the potential changes induced by IMF By.

Figure. 3. Correlation in a running 27-day interval between the daily mean downwelling infrared irradiance (D_IR) and the upwelling irradiance (U_IR) measured at Alert, Canada 2004-2015.

Figure 4. Lagged correlations for all seasons and all sector types of D_IR and U_IR with (-By), blue and orange curves respectively; and with VpN, green and red curves respectively.

Figure 5. Lagged correlations for each October through April and all sector types of D_IR and U_IR with (-By), blue and orange curves respectively; and with VpN, green and red curves respectively.

Figure 6. Lagged correlations for Octobers through Aprils of D_IR and U_IR with VpN for 2 & 4 sector solar wind intervals, 2004-2015.

Figure 7. Lagged correlations of 2-sector U_IR values with VpN for October-April intervals. 2007-2009 (orange) and 2010-2015 (blue) with the overall correlation in black.

Figure 8. Lagged correlation with VpN for isolated -7d to +7d portions of + to – sectors of Alert irradiance data, 2004-2015. For October-March intervals for the combined 2&4 sectors, D_IR (grey) and U_IR (yellow); and for just 2-sectors, D_IR (orange) and U_IR (green).

Figure 9. Lagged correlation with VpN for isolated -7d to +7d portions of – to + sectors of Alert irradiance data, 2004-2015. For October-March intervals for the combined 2&4 sectors, D_IR (grey) and U_IR (yellow); and for just 2-sectors, D_IR (orange) and U_IR (green).

Figure 10. Superposed epoch analyses of changes in Alert irradiances and VpN across 2&4, + to -, sector boundaries. D_IR (blue). U_IR (green) can be compared to VpN/3 (red). October - March, 2004-2015. The units of irradiance are W/m^2. Ten units of VpN/3 correspond to 30 kV of the ionospheric potential change.

Figure 11. Superposed epoch analyses of changes in Alert irradiance and VpN across 2&4 sector, – to + sector boundaries. D_IR (blue). U_IR (green) can be compared to VpN/3 (red). October - March, 2004-2015. The units of irradiance are W/m^2. Ten units of VpN/3 correspond to 30 kV of the ionospheric potential change

Figure 12. Lagged correlations of surface pressure in the same format as Fig 4 with (-By), VpN, and SigmaN, for October-March intervals 1995-2018. Only the 2 & 4-sector intervals of solar wind structure were used.

Figure 13. Lagged correlation of the zonal mean pressure 81-71N with SigmaN for 2&4 sector intervals 1995-2018. The northern summer months, June-July, are in blue, and the cold season, October-March, are in red.

Figure 14. Lagged correlations for the band from 90°N to 71°N with SigmaN, with the data for pressure responses to 4-sector intervals (blue) separated from those to 2-sectors (orange). Oct-March intervals, 1995-2018.

Figure 15. Comparison of lagged correlations of with SigmaN for 2&4 solar wind sectors in three 10° wide latitude bands for October-March intervals 1995-2018.

Figure 16. Lagged correlation of pressure band 90°-71°N with SigmaN, for 2-sector October-March intervals. December 1998 - March 2004 (blue); October 2007 - February 2015 (green); October 2015 - March 2017 (orange).

Figure 17. Lagged correlations for isolated -7d to+7d portions of + to - sectors, 2005-2018. For 90°-71°N 2-sector (grey) and 4-sector (orange). For 51°-31°N 2-sector (green) and 4-sector (blue).

Figure 18. Lagged correlations for isolated -7d to +7d portion of - to + sectors, 1995-2018. . For 90°-71°N 2-sector (grey) and 4-sector (orange). For 51°-31°N 2-sector (green) and 4-sector (blue).

Figure 19. Superposed epoch analysis of pressures 90°-71°N 2s&4s (green), 2s (orange); 51°-31°N 2s&4s (grey), 2s (blue) across sector boundaries for + to – VpN changes; also of (VpN/2+2) (red). October-March, 1995-2018. Ten units of VpN/2 correspond to 20 kV of ionospheric potential change.. For the pressure·area values, 10 units on the plots corresponds to about 2 hPa for the 90°-71°N band, and about 0.4hPa for the 51°-31°N band.

Figure 20. Superposed epoch analysis of pressures 90°-71°N 2s&4s (green), 2s (orange); 51°-31°N 2s&4s (grey), 2s (blue) across sector boundaries for + to - VpN changes. Ten units of VpN/2 correspond to 20 kV of ionospheric potential change. For the pressure·area values, 10 units on the plots correspond to about 2 hPa for the 90°-71°N band, and about 0.4hPa for the 51°-31°N band.

Figure 21. Flow chart of inputs and links influencing atmospheric electric interactions with clouds. Links involving deposition of electric charge on droplets and aerosol particles, influencing the microphysical electro-scavenging and electro-anti-scavenging processes in clouds, are shown in heavier lines.

Figure B1. Solar wind–induced potential distributions over the northern polar cap as functions of magnetic latitude and magnetic local time. The data is from the empirical model of satellite observations by Weimer (1996). In each case the total IMF is 5 nT and the solar wind speed Vsw = 450 kms^{-1}. The four seta are for four different combinations of IMF By and IMF Bz, with (a) and (c) for positive By and (b) and (d) for negative By. With (a) and (b) the Bz component is negative, while for (c) and (d) it is positive, as indicated on the clock angle insert.

Figure B2. The solar wind induced potential at the north magnetic pole, for the six sets of B_T, Vsw and clock angles listed in Table 1. The value of By (horizontal axis) and Bz (vertical axis) for a given B_T determine the clock angle θ. If both are positive, θ = $\tan^{-1}$ (By/Bz).

Figure B3. Integrals of potential over the area of the polar cap are given as a function of clock angle for B_T values 5 nT, 7.5 nT, and 10 nT, with Vsw values of 300, 450, and 800 kms^{-1}. In (a) the integral is only over negative potentials, while in (b) it is over positive potentials, and in (c) the integral is over the whole polar cap (algebraic sum of (a) and (b). The positive lobe in (c) is shown in expanded scale in (d).